The guide RNA sequence dictates the slicing kinetics and conformational dynamics of the Argonaute silencing complex

Peter Y. Wang[1,2,3], David P. Bartel[1,2,3,4,*]

[1] Whitehead Institute for Biomedical Research, 455 Main Street, Cambridge, MA, 02142, USA

[2] Howard Hughes Medical Institute, Cambridge, MA, 02142, USA

[3] Department of Biology, Massachusetts Institute of Technology, Cambridge, MA, 02139, USA

[4] Lead contact

* Correspondence: dbartel@wi.mit.edu

SUMMARY

The RNA-induced silencing complex (RISC), which powers RNA interference (RNAi), consists of a guide RNA and an Argonaute protein that slices target RNAs complementary to the guide. We find that for different guide-RNA sequences, slicing rates of perfectly paired, bound targets can be surprisingly different (>250-fold range), and that faster slicing confers greater knockdown efficacy in cells. Four sequence determinants underlie much of this variation in slicing rates. Analyses of these determinants implicate a structural distortion at guide nucleotides 6–7 in promoting slicing, and indicate that, in contrast to the prevailing model, slicing is primarily limited by the rate at which the enzyme−substrate complex reaches a slicing-competent conformation. Moreover, different guide sequences have an unanticipated, 600-fold range in 3′-mismatch tolerance, which is attributable to the GC-content of their central regions. Together, our analyses identify sequence determinants of RISC activity and provide biochemical, conformational, and functional rationale for their action.

KEYWORDS

RNAi, Argonaute, AGO2, RISC, slicing, microRNA, siRNA, kinetic analysis, RNA–protein interactions

INTRODUCTION

Argonaute (AGO) proteins are found in animals and most other eukaryotes, as well as some bacteria and archaea.[1] In eukaryotes, AGO proteins typically mediate the post-transcriptional silencing of target RNAs based on their complementarity to an associated guide RNA, which can be either a microRNA (miRNA) or a small interfering RNA (siRNA).[2–4] MicroRNAs are derived from short RNA hairpins, whereas endogenous siRNAs are derived from longer, double-stranded RNAs.[5] Chemically synthesized guide RNAs are also called siRNAs.[6] Nevertheless, regardless of its origin, any guide RNA loaded into an AGO protein is able to access the functional repertoire of that AGO.[7,8] In metazoans, function depends on the extent of pairing to the guide RNA. Pairing that is less-extensive, often involving perfect pairing to only the guide-RNA seed region (guide-RNA nucleotides 2–8), leads to recruitment of TNRC6, which in turn recruits deadenylation complexes, ultimately causing degradation and/or translational repression of the target transcript,[9] whereas pairing that is extensive can also lead to AGO-catalyzed endonucleolytic slicing of the target transcript.[10–12]

Slicing is the biochemical basis of RNA interference (RNAi), which provides defense against viruses and transposable elements for many eukaryotic species. In this context, a slicing-competent AGO, together with its guide RNA, is called an RNA-induced silencing complex (RISC).[13] Of the four mammalian AGO paralogs, AGO2 is the one most adept at catalyzing slicing.[10,12,14] In mammals, 20 miRNAs direct the AGO2-catalyzed slicing of 24 transcripts,[15–18] and in mice, endogenous siRNAs also direct slicing required for oocyte meiotic maturation.[19] Slicing is also required for the biogenesis and maturation of at least two miRNAs[20–23] and most siRNAs.[24–26] Finally, slicing is key to potent knockdown directed by synthetic siRNAs, which are used extensively in biomedical research and increasingly applied to treat disease, with the recent clinical approval of five new siRNA-based therapies.[27]

The slicing conformation was initially proposed to occur through a two-step process, in which pairing nucleates at a pre-organized guide-RNA seed region and then propagates contiguously until reaching the guide 3′ region.[3,28–30] Aided by crystal structures and single-molecule kinetics, this model was elaborated to three steps, starting with initial pairing to pre-organized nucleotides 2–5, followed by pairing to the remainder of the seed, enabled and reinforced by repositioning of AGO helix-7, followed by the zippering of the pairing from the seed to the remainder of the guide.[31–34] A concern regarding these early models is that contiguous propagation of pairing from a stationary seed to form ~20 pairs, in which the guide RNA has wrapped nearly twice around the target, poses a serious topological challenge.[28] To circumvent this challenge, the current model proposes a second nucleation event that facilitates pairing

propagation.[2] In this current, four-step model, the two steps of seed pairing are followed by nucleation of a second guide−target helix at the 3′ supplementary region of the guide, which centers at positions 13−16 (step 3), followed by propagation of this second helix in both directions (step 4).[2] Propagation to the end of the guide dislodges the guide 3′ end from the PAZ domain of AGO, which enables rotation of this second duplex and its migration into the central cleft of AGO. The rotation and movement of this second helix enable pairing to propagate into the guide central region (positions 9–12), ultimately completing a continuous RNA double helix (Figure S1A). This final conformational change, involving pairing of the central region, is presumably a limiting factor for slicing. Recent structures support this four-step model,[35,36] as does the observation that eliminating the AGO N and PAZ domains allows rapid and promiscuous slicing.[37,38]

Biochemical studies of RISC have measured kinetic parameters and defined base-pairing requirements of slicing guided by either let-7a or miR-21.[34,39–42] However, the extent to which these findings generalize to a wider variety of guide-RNA sequences has been unclear. Indeed, less thorough analyses of RISC guided by other RNAs suggest that guide-RNA identity might influence slicing efficiency.[32,43] Likewise, the guide RNAs in high-resolution structure models have been limited to only a few sequences, and the impact of guide-RNA sequences on the conformational dynamics of AGO2 has remained largely unknown.

In this work, we measured the slicing kinetics of AGO2 loaded with a variety of guide RNAs. We found that the sequence of the guide RNA not only influences the binding of the target and sliced products but also dictates the conformational dynamics of target-bound RISC and consequently the rate of slicing, thereby affecting the efficacy of RNAi in cells.

RESULTS

The rate of target association can obscure slicing kinetics

To explore how the guide-RNA sequence influences AGO2-catalyzed slicing, we measured the slicing kinetics of AGO2 loaded with 13 different miRNAs, most of which had been either previously biochemically studied or shown to carry out cellular slicing-mediated functions.[14,15,18,39,43,44] Each of the 13 RISCs were generated in cellular extracts, purified by antisense capture and affinity elution,[45] and quantified using stoichiometric binding of radiolabeled RNA by limiting amounts of the complex (Figures S1B and S1C). Slicing kinetics of each RISC were then measured using in vitro single-turnover slicing assays, with RISC in excess of a radiolabeled target RNA harboring a

perfectly complementary site for the miRNA (Figure 1A). At each time point, the reaction was quenched and unsliced substrate and sliced product were resolved on denaturing gels and quantified (Figure 1B).

The use of single-turnover conditions, with enzyme in excess over substrate, coupled with slow dissociation of fully paired substrate,[34] ensured that the reaction kinetics would not be perceptibly influenced by the rates of either product release or substrate dissociation and instead would be influenced by the rates of substrate association and/or slicing, as described by the elemental rate constants k_{on} and k_{slice}, respectively (Figure 1C). Previous analyses of AGO2 associated with either let-7a or miR-21 show that under typical experimental concentrations of RISC, slicing is slower than association, such that the apparent single-turnover reaction kinetics correspond to the rate-limiting k_{slice} (Figure 1C).[39,42] However, for some other miRNAs that we tested, the reaction kinetics increased with RISC concentration, indicating some contribution by the second-order association kinetics, i.e., by k_{on} (Figure 1D). To separate the contribution of k_{on} from that of k_{slice}, for each miRNA, we conducted the assay at multiple RISC concentrations and fit the combined results to a simplified ordinary differential equation (ODE) model that included both association and slicing kinetics (Figure 1E).

To validate the results of our ODE model, we used filter-binding to separate the bound target RNA from free target RNA at different time points (Figures S2A and S2B). At early time points, partial binding of target RNA was observed for miRNAs that had slower association kinetics in our slicing assays but not for those that had faster association kinetics (Figure S2C). These results also confirmed that, as assumed in our modeling, fraction-sliced endpoints falling below 100% could be attributed to a small fraction of defective enzyme (Figures S2E−G). To orthogonally confirm that the ODE model produced accurate k_{on} values, we directly measured the association kinetics using filter-binding assays of target RNAs harboring central mismatches, which cannot be sliced. As expected, k_{on} values obtained from filter-binding measurements corresponded to the k_{on} values obtained from ODE modeling of the slicing data (Figure S3A).

The association kinetics of RISCs corresponded to the predicted standard free energy ($\Delta G°_{37°C}$) of RNA secondary structure at the seed-matched region of the target site (Figures S3B−D), which supported the idea that the secondary structure of the target occludes the binding of RISC.[32,44,46–49] Moreover, association kinetics did not correlate with the slicing kinetics (Figure S3E), which indicated that we were able to disentangle them from each other to generate accurate k_{slice} values for a broad range of miRNAs, enabling investigation of the interplay between miRNA sequence and k_{slice} values (Figure S4; Table S1).

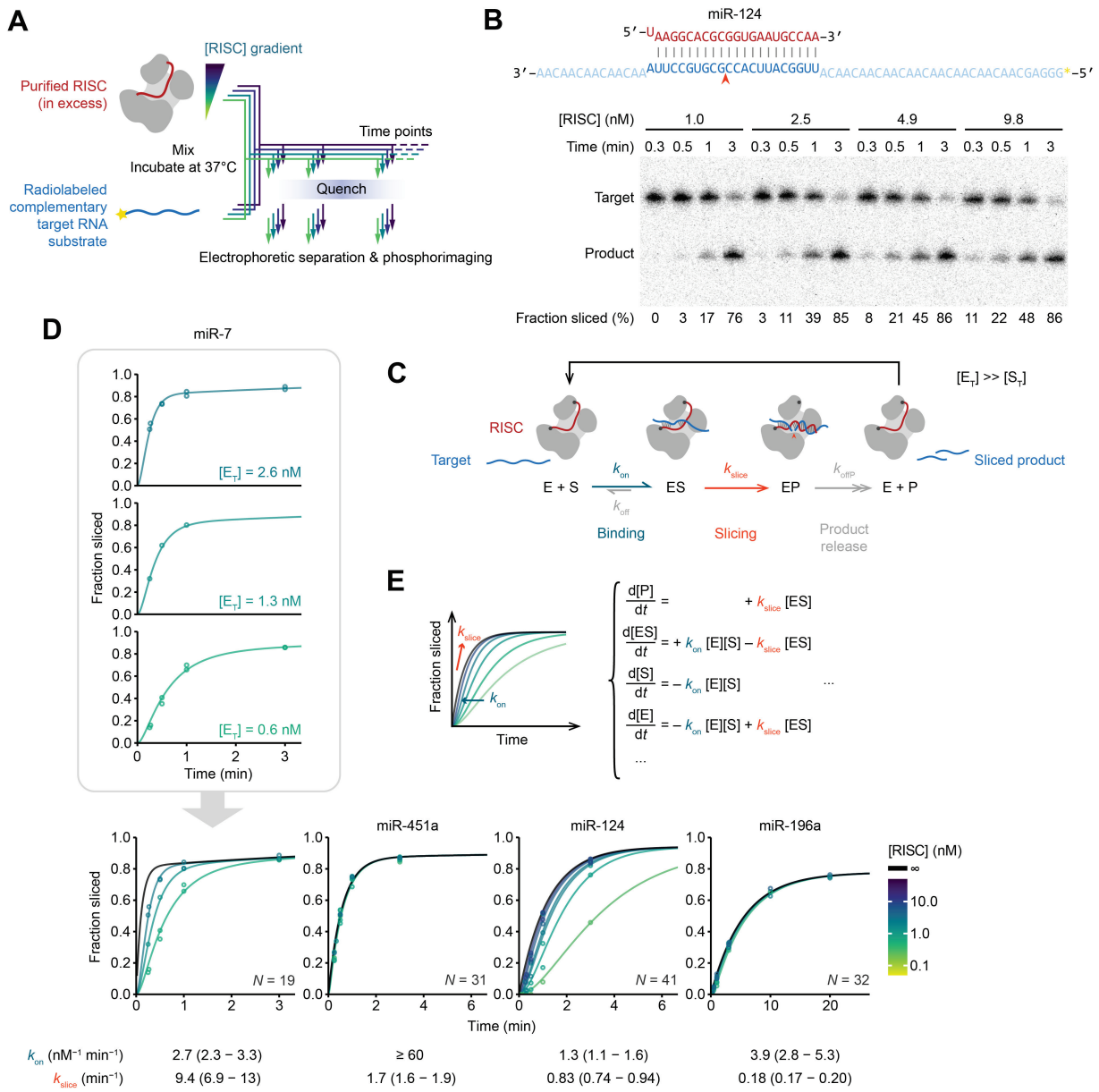

Figure 1. Precise measurement of RISC-catalyzed slicing kinetics

(A) Schematic of in vitro single-turnover slicing assay using purified RISC. The guide is shown in red, AGO2 in gray, and target in blue, with its ^{32}P radiolabel indicated with a yellow star. Reactions with increasing concentrations of RISC are depicted as a gradient from green to purple.

(B) Representative results of miR-124-directed slicing of a perfectly complementary target. The site of slicing is indicated (orange caret); otherwise, colors are as in (A). The initial target concentration was 0.1 nM, and the fraction of target sliced is indicated below each lane.

(C) Minimal kinetic scheme of binding and slicing. Colors are as in (A). The active site of AGO2 is indicated with an orange caret. E represents the RISC, S represents the target substrate, and P represents the sliced product. For the single-turnover reactions of this figure, RISC is in excess and at high concentrations, and thus product release and substrate dissociation (both shown in gray) play negligible roles.

(D) Representative results from slicing assays using four different miRNAs. Data points and associated reaction curves from ODE model-fitting are plotted in a gradient from green to purple for increasing concentrations of RISC. The extrapolated reaction curve at infinite RISC concentration, which represents a reaction rate determined purely by slicing kinetics, is plotted in black. Results at time points beyond the limits of the x-axes are not shown. The total number of data points measured for each miRNA is indicated as *N*. Values of k_{on} and k_{slice} obtained from ODE model-fitting for each miRNA are shown below. Ranges in parentheses indicate 95% CIs from model-fitting. Binding rate for miR-451a was too fast to resolve in our assays and was thus set to the diffusion limit (60 nM^{-1} min^{-1}). All miRNAs were 22-nt long, unless otherwise stated.
(E) Simplified ODE model describing the reaction equation in (C), with a schematic kinetic plot demonstrating the contribution from each kinetic parameter. Colors are as in (C) and (D).
See also Figures S1, S2, S3, and S4.

miRNA sequence can confer >250-fold differences in k_{slice} values of perfectly paired targets

When presented with their perfectly matched targets, the 13 characterized RISCs had k_{slice} values spanning >250-fold, with the half-life of slicing spanning 4.4 s (95% confidence interval [CI], 3.3–6.1 s) to 19 min (95% CI, 18–20 min) (Figure 2A). Examining the sequences of the 13 miRNA guide RNAs suggested that nucleotide identities at three positions were potentially associated with increased k_{slice} values. These included a preference for purine (R) at position 10, and a preference for an A or U (W) at positions 7 and 17 (Figure 2A).

To test these candidate sequence determinants, we made single-nucleotide substitutions at these positions and measured their impact on k_{slice} for the corresponding perfectly paired target RNAs. The purine/pyrimidine identity at position 10 most strongly affected k_{slice}, conferring an 8.2- or 9.4-fold difference when changing to a purine or vice-versa (Figures 2B and 2C). Changing position 17 to or from an A or U had a 2.1- or 6.3-fold effect on k_{slice} (Figure 2C), and changing position 7 from an A to a G reduced k_{slice} 4.4-fold, whereas changing it from a G or C to an A increased k_{slice}, albeit modestly (1.1- or 1.5-fold) (Figure 2C). Triple mutants with concordant substitutions at all three determinants imparted a 4.7- or 51-fold difference in k_{slice}, further validating these sequence features (Figure 2C). These changes in k_{slice} were generally greater than the variation found in the measurements of biological replicates, which indicated that these were bona fide effects of the substitutions (Figure S5A). Moreover, most of these effects on k_{slice} were far stronger than that of a phosphomimetic substitution of serine-387 of the AGO2 protein (Figures S5B and S5C), a residue that, when phosphorylated, is reported to downregulate slicing-mediated repression in cells.[50]

Shorter guide lengths can introduce stronger tension at the miRNA 3′ terminus upon pairing to the miRNA 3′ region.[35] Reasoning that this tension might favor the

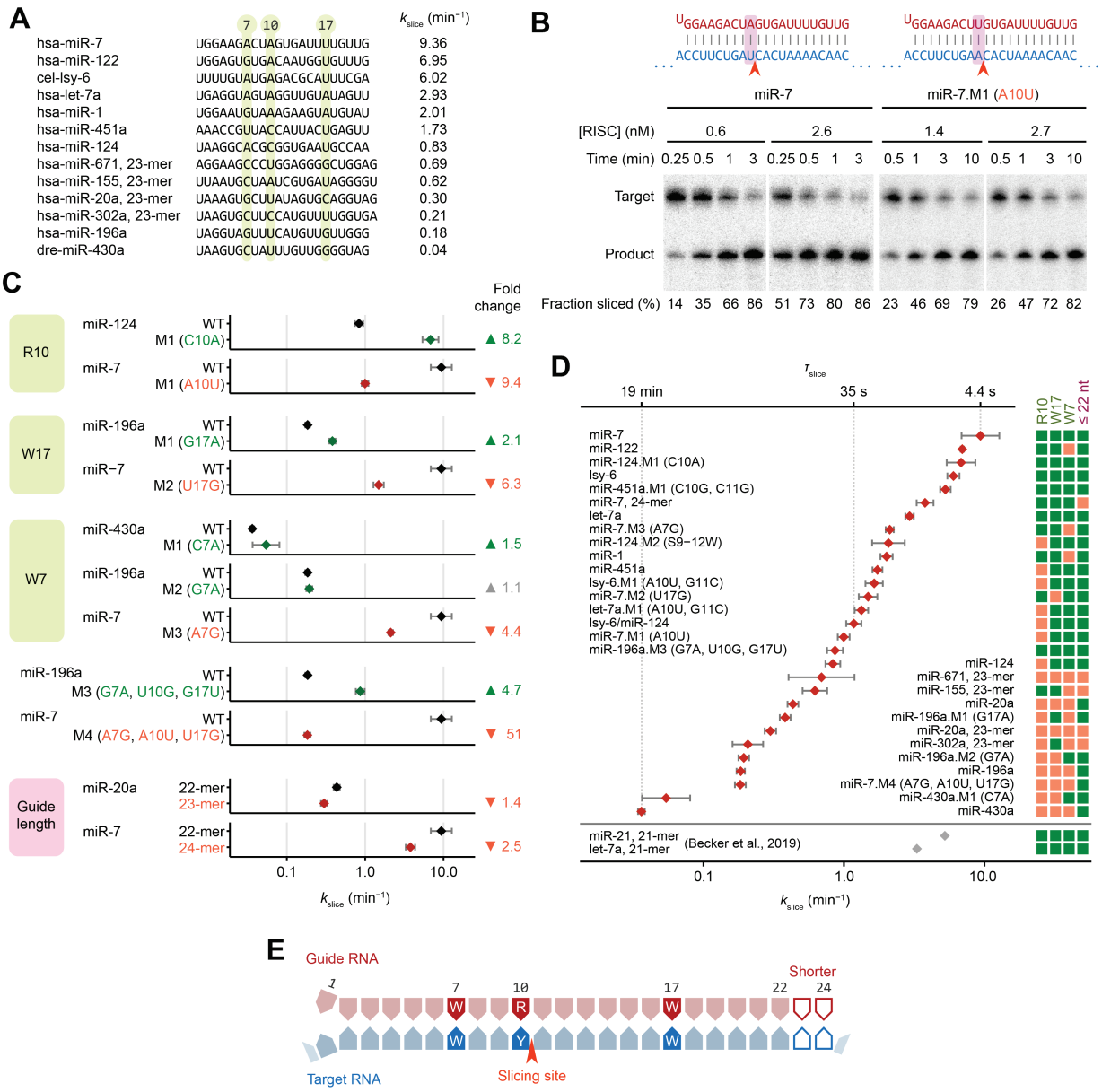

Figure 2. Guide-RNA sequence determinants that underlie variation in slicing kinetics

(A) A broad range in k_{slice} values. Listed are the 13 initially tested miRNAs and their k_{slice} values, in decreasing order. Positions of candidate sequence determinants are highlighted in green.

(B) Effect of substituting the base pair at position 10. Shown is a representative analysis of a wildtype miRNA (miR-7) and its mutant (miR-7.M1), in which the A at position 10 was substituted with U (A10U). The initial concentration of target RNA was 0.05 nM in these assays; otherwise, as in Figure 1B.

(C) Validation of sequence determinants through base-pair substitutions and additions. Results for wildtype–mutant pairs used to interrogate each sequence determinant are grouped together, with the sequence determinant indicated on the left. Results for triple mutants of miR-196a and miR-7, each with substitutions at positions 7, 10, and 17, are also shown. The measured k_{slice} values are plotted in log-scale, with error bars indicating 95% CIs from model-fitting. Wildtype values are in black; those for substitutions expected to increase or decrease k_{slice} are in green and orange, respectively. Relative fold

changes observed between wildtype and mutants are indicated on the right (with the fold change that was smaller than the 95% CI of biological replicates shown in gray).
(D) k_{slice} values for perfectly complementary targets for all 29 guide RNAs tested in this study. k_{slice} values are plotted as in (C), with the top axis also showing the corresponding half-life values for slicing (τ_{slice}), labeling the minimum, maximum, and median values. For reference, k_{slice} values from a previous study[39] are shown at the bottom. On the right, green indicates the presence of a favorable determinant, and orange its absence.
(E) Summary of determinants identified for k_{slice} of perfectly complementary target substrates. Colors are as in (B).
See also Figure S5.

release of the 3′-end of the guide, which is a conformational requisite of slicing,[30] we measured k_{slice} values of different length isoforms for two guide RNAs and found small but consistent increases in k_{slice} for shorter guides (Figure 2C).

Together, these results experimentally supported the identification of four determinants that influence the slicing step of perfectly paired target RNAs. They were, in decreasing order of effect size: (1) a purine at miRNA position 10, (2) an A or U at miRNA position 17, (3) an A or U at miRNA position 7, and (4) a shorter miRNA (Figures 2C−E). Moreover, the >250-fold range in k_{slice} values observed for perfectly complementary sites of different guide RNAs extended two orders of magnitude below the two-fold range previously reported (Figure 2D)[39] and indicated that AGO2 k_{slice} values span a much larger range and are often slower than previously appreciated.

k_{slice} can limit multiple-turnover catalysis

Previous work with let-7a shows that the rate of multiple-turnover catalysis by AGO2 is limited by the rate of product release (k_{offP}), especially when the target is extensively complementary to the guide.[34,40,41] The wide dynamic range of k_{slice} values observed for other miRNAs suggested that, for some, slicing might be rate-limiting in multiple-turnover conditions, even for fully paired targets. To test this possibility, we conducted multiple-turnover slicing assays for several guide RNAs to measure their k_{offP} values and reaction kinetics. Although some miRNAs, such as miR-7.M1, exhibited burst-phase kinetics indicative of k_{offP}-limited catalysis, others, such as miR-196a.M3, exhibited single-phase kinetics limited by k_{slice} throughout multiple rounds of catalysis, which indicated that k_{offP} exceeded k_{slice} (Figures S5D and S5E). These results showed that, depending on the miRNA sequence, either slicing or product release can dictate the maximal catalytic rate constant of AGO2.

Sequence determinants that enhance k_{slice} promote greater knockdown efficacy in cells

In-cell functional screens have identified siRNA sequence features that confer greater knockdown efficacy, which have since served as guidelines for designing new siRNAs[51] (Figure S5F). Although some of these features have been attributed to either more efficient maturation of RISC[52,53] or increased structural accessibility of the target sites,[54] three features have remained mechanistically unexplained. Remarkably, these three features precisely aligned with the three k_{slice} determinants that we observed at positions 7, 10, and 17 (Figure 2E, S5F), which implied that improved AGO2 slicing kinetics underlie the functional efficacy of siRNAs bearing these three sequence features.

To validate the functional impact of the k_{slice} sequence determinants on RNAi efficacy, we designed a dual-luciferase reporter assay to test the effect of these sequence determinants on the knockdown of target transcripts in cells (Figure 3A). Specifically, we tested two pairs of wild-type and mutant miRNAs, in which the mutant miRNAs had concordant single-nucleotide substitutions at positions 7, 10, and 17 shown to either reduce or increase k_{slice} (Figure 3B). For each guide RNA tested, we placed the corresponding perfectly complementary site within two different open-reading-frame (ORF) contexts (either a 3xFLAG-tagged GFP or a 3xHA-tagged human-orthogonal SUMO). The translation rates of these ORFs were placed under control of an iron-response element (IRE), such that the translation initiation rate could be tuned by the addition of either iron or an iron chelator[55] (Figures 3A and 3C), which enabled testing of whether kinetic competition by translocating ribosomes expected to clear bound RISCs might contribute to the benefit of faster slicing kinetics.[56] Effects on reporter RNA levels were monitored using destabilized NanoLuc luciferase translated from a downstream ORF under translational control of an EMCV internal ribosome entry site (IRES), such that NanoLuc activity reported on the levels of the reporter transcript without sensitivity to IRE modulation of cap-dependent translation initiation (Figure 3A).

In both HeLa and HEK293T cells, across both reporter sequence contexts, and for both pairs of guide RNAs tested, the faster-slicing guide variant usually achieved significantly greater target knockdown (Figure 3D). The smallest differences were observed for miR-7 in HEK293T cells, which can be attributed to the relatively high levels of endogenous miR-7 in HEK293T cells,[57] which would be expected to diminish the effect of transfected miR-7. Interestingly, neither a global change in knockdown efficacy nor an additional advantage of fast-slicing guides was observed when translation through the site of cleavage was substantially increased (Figures 3C and 3D), which suggested that, at least in the context of our reporter assays, AGO2-mediated slicing was not subject to a kinetic competition against translocating ribosomes.

A lack of enhanced knockdown following increased translation of rapidly sliced sites also implied that increased target accessibility due to the removal of secondary structures by translocating ribosomes did not improve knockdown efficacy, which suggested that target unfolding might not be rate-limiting for these sites, despite trends observed for a different set of slicing sites.[58] Most importantly, these results validated the functional link between k_{slice} sequence determinants and RNAi efficacy in cells.

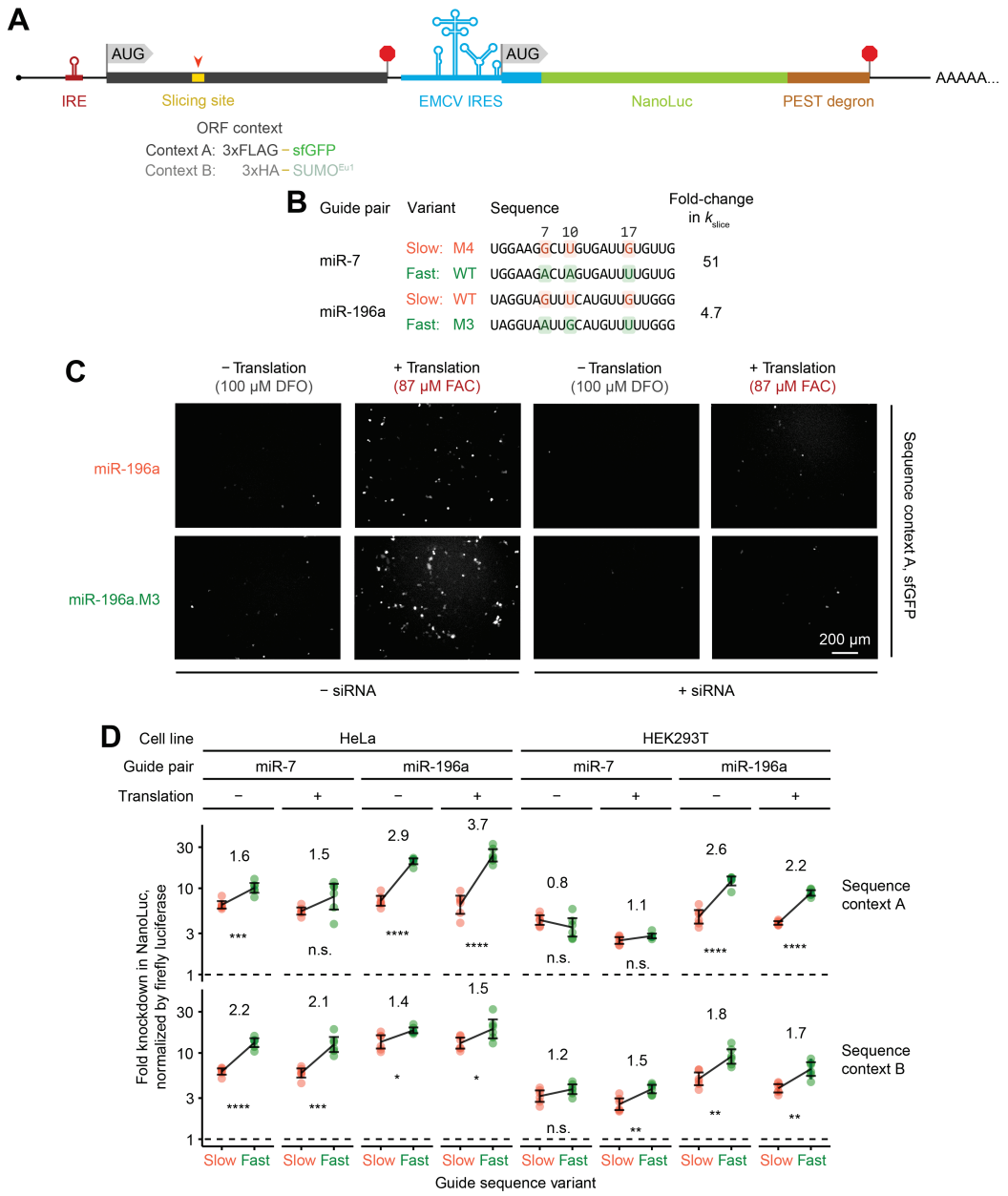

Figure 3. Favorable sequence determinants confer stronger knockdown in cells
(A) Schematic of reporter constructs. Thicker bars indicate ORFs; thinner bars indicate RNA elements; AUGs indicate start codons; stop signs indicate stop codons, and the orange caret points to the perfectly

complementary site for slicing (in yellow). The slicing site resided in one of two different ORF contexts—either context A, in which the slicing site was positioned between a region coding for the 3xFLAG-tag and a region coding for superfolder GFP (sfGFP),[81] or context B, in which the slicing site was positioned between a region coding for the 3xHA-tag and a region coding for human-orthogonal SUMO protein ($SUMO^{Eu1}$).[82]
(B) Sequences of four guide RNAs tested with the reporter assays, shown as two pairs of wildtype and mutant sequences. Key features of the slower-slicing variant are in orange, and those of the faster-slicing variant are in green.
(C) Representative fluorescent microscopy images of HEK293T cells transfected with reporter constructs in which the slicing site was in ORF context A, which contained the sfGFP domain. Cells were imaged after 17 h of treatment with either iron chelation (desferroxamine; DFO) or iron (ferric ammonium citrate; FAC). Scale bar is in the bottom right; all images were acquired at the same magnification.
(D) Reporter evidence for greater knock-down by miRNAs with more favorable slicing determinants. Plotted are reporter knockdown efficacies observed with the indicated cell lines, treatments, and reporter contexts. The fold differences observed between the mean knockdown values of the slow and fast guide variants are shown above each set of data points. Each error bar indicates the 95% CI of the geometric mean across six biological replicates. Significance, as measured using the unpaired two-sample *t*-test, calculated in log-scale for fold-change values, is indicated below each set of data points (**** $p < 0.0001$, *** $p < 0.001$, ** $p < 0.01$, * $p < 0.05$, n.s. not significant). Colors are as in (B).

Weak pairing around positions 6−7 appears to facilitate a helical distortion associated with pairing beyond the seed

We next sought to identify the structural basis by which sequence determinants might influence slicing kinetics, with particular interest in the determinants at positions 7 and 17, which were distant from the cleavage site. With respect to enhanced slicing associated with an A:U or U:A pair at position 7, we hypothesized that this might be imparted through the same mechanism as the enhanced slicing previously observed for a G:G mismatch at position 6,[43] and that this unknown mechanism might involve weak pairing at positions 6 or 7. To test this hypothesis, we investigated how enhancement by a position-6 G:G mismatch was affected when the pair at position 7 was changed. In the context of miR-7.M3, which makes a disfavored G:C base-pair at position 7, introducing a G:G mismatch at position 6 increased k_{slice} by 2.4-fold (Figures 4A and 4B). In contrast, this enhancement was absent in the context of miR-7, which already makes a favored weak A:U base-pair at position 7. Moreover, when comparing slicing directed by miR-7 and miR-7.M3, the effect from the substitution at position 7 diminished from 4.4-fold to 1.9-fold in the context of the G:G position-6 mismatch (Figures 4A and 4B). Thus, the enhancement of k_{slice} by the weak pair at position 7 and by the G:G mismatch at position 6 were non-additive and at least partially redundant, as expected if they were mediated through the same mechanism. In contrast, an analogous comparison using substitutions at positions 10−11 found no significant impact on the enhancement of k_{slice}

by the position-6 mismatch, as expected if the determinants were acting independently (Figures S6A and S6B).

To further test the idea that the weak pair at position 7 and the G:G mismatch at position 6 were not exerting their influence through separate mechanisms, we tested target RNA substrates with a G:G mismatch at position 7. A G:G mismatch at position 7 of miR-7.M3 enhanced k_{slice} by 1.9-fold, similar to its effect at position 6 (Figures 4A and 4B). In comparison, a G:G mismatch at position 7 of miR-196a did not enhance k_{slice}, which resembled the lack of effect from mutating a G:C base-pair to an A:U base-pair at position 7 of miR-196a (Figures 4A, 4B, and 2C), providing further evidence that the enhancement of k_{slice} by the position-7 sequence determinant was related to the enhancement by G:G mismatches at positions 6 and 7, as expected if they were mediated through the same mechanism.

We hypothesized that slicing might require a structural distortion around positions 6 and 7, which a weaker or disrupted base-pair might favor. To investigate this idea, we analyzed five high-resolution structure models of slicing-competent AGO proteins, including four of human AGO2 and one of *Arabidopsis thaliana* AGO10, in which different types of target RNAs were engaged. These included structures with either 1) no target,[59] 2) a target paired to only the seed region,[59] 3) a target paired additionally to positions 13−16,[35] 4) a target paired more extensively to the 3′ half of the guide,[60] or 5) a target paired perfectly from positions 2–16.[36] Examining the dihedral angles of the guide-RNA backbone in these structure models revealed a striking difference in the three structures with pairing beyond the seed; these three each had a clear local deviation from the A-form double helix between positions 6 and 7 (Figure 4C; Figures S6C and S6D). Although the vast majority of ribose rings at well-resolved nucleotides in the miRNA had C3′-endo geometry, typical of A-form RNA, for these miRNAs pairing beyond the seed, the ribose ring at position 6 had a distinct C2′-endo geometry, which was evident from the deviated δ and ν_2 dihedral angles and electron density maps (Figures 4C and 4D; Figure S6C). Consequently, the RNA backbone adopted a kink between positions 6 and 7, as reflected in the distinct γ dihedral angles and conformer classes (Figure 4C; Figure S6D), and this distortion resulted in a 3.8-Å shift in the position of the guide at position 7 (Figure 4E). Based on these observations, we posit that this distortion is necessary for the correct positioning and register of the guide−target double helix for base-pairing and slicing, and that it may be favored by a weak or mismatched base-pair at positions 6 or 7. Supporting this model, incorporation of a flexible (*S*)-glycol nucleic acid (*S*-GNA) backbone modification at position 6 or 7 but not at any other positions of the guide or passenger strand enhances knockdown efficacy of siRNAs in cells.[61,62] Indeed, the authors of the *S*-GNA study note that the

beneficial effect of *S*-GNA corresponds to the site of distortion observed in the structures. Together, our studies suggest that favoring this distortion acts to increase k_{slice}, as presumably occurs for optimized *S*-GNA-containing siRNAs currently in the clinic, illustrating the apparent clinical utility of this proposed mechanism.

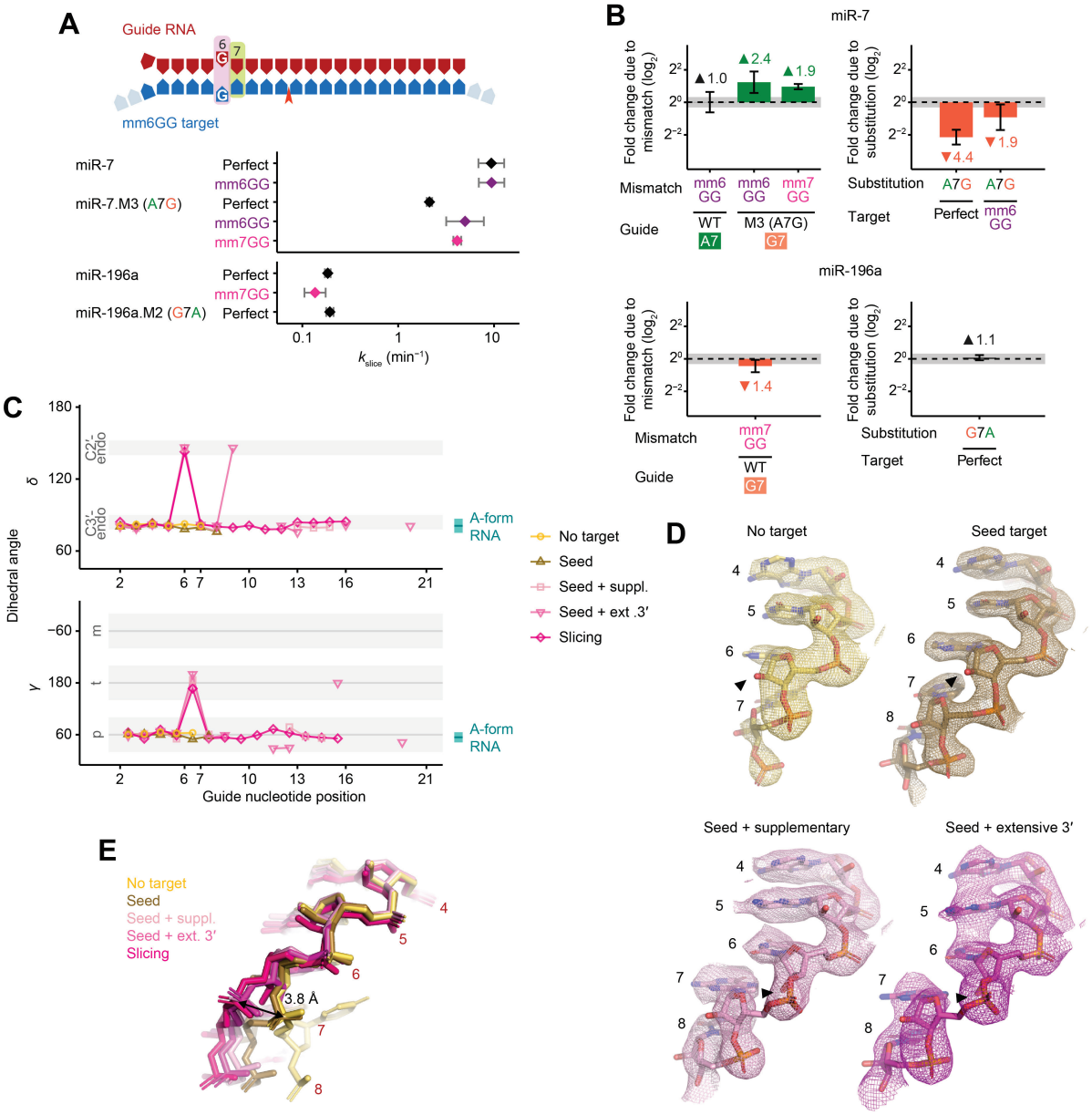

Figure 4. Enhancement of slicing by a weak pair or mismatch at positions 6−7 aligns with local backbone distortion

(A) Effects of mismatches at positions 6–7. The schematic illustrates base-pairing with a G:G mismatch at position 6, highlighting positions 6 and 7; otherwise, as in Figure 2E. Measured k_{slice} values show the effects of mismatches in different contexts; otherwise, as in Figure 2C.

(B) Comparisons of k_{slice} values observed in (A), plotted in log-scale. Left panels show the fold change in k_{slice} due to different mismatches in the target, in the context of different guide RNAs. The nucleotide identity at the position-7 sequence determinant is indicated for each guide. Right panels show the fold change in k_{slice} due to substitutions introduced at position 7, in the context of either perfectly complementary targets or targets harboring a mismatch at position 6. Fold change values are also indicated above or below the bar plots. Error bars indicate 95% CIs after propagating uncertainty from model-fitting for the two k_{slice} values compared. Colors are as in (A) and Figure 2C. The 95% CI of expected background variation is indicated with gray shading (Figure S5A).
(C) Changes in δ and γ dihedral angles observed in the guide backbone as RISC assumes different conformational states. Measurements are from structure models in which the guide RNA has either no target (4W5N, yellow), seed-pairing (4W5R, brown), seed and supplementary-pairing (6N4O, light pink), seed and extensive 3′-pairing (6MDZ, magenta), or perfect pairing from position 2 to 16 (7SWF, deep pink). Values are only shown for base-paired nucleotides or, in the case of the no-target state, positions 2−7, which are pre-organized into A-form-like helix by AGO. Six values corresponding to unexpected conformation outliers, indicating possible poor model-fit, were found in positions 13−19 of either the state with seed and supplementary pairing state or the state with seed and extensive 3′-pairing state; these were not plotted (Figure S6D). Expected ranges of angles for canonical conformers are shown in gray, and expected ranges of angles for A-form helices are indicated in turquoise on the right.[83]
(D) A distortion of the guide RNA backbone as RISC assumes different conformational states. Shown are structure models of the guide backbone at positions 4−8 for each of the structures in (C) that were solved using crystallography, overlaid with electron density omit maps ($2mF_o - DF_c$)[84] contoured at 1.6 σ, shown in mesh. The 2′-hydroxyl of position 6 is indicated with a black triangle for each model. For the no-target state position 8 was not resolved and is therefore not shown. Colors are as in (C).
(E) As in (D) but for all five structure models and without the electron density maps. Models were overlaid and aligned at MID and PIWI domains of AGO. Displacement of the position 7 phosphate observed as RISC shifts from the no-target state to the slicing state is indicated with an arrow.
See also Figure S6.

Rapid slicing of terminally mismatched sites is associated with strong predicted central pairing

The preference for an A:U or U:A pair at position 17 prompted examination of slicing kinetics of targets harboring mismatches at this position. In contrast to mismatches at positions 6 or 7, mismatches at positions 17 strongly disrupted slicing. Indeed, for seven cases tested, each in the context of either miR-7, miR-196a, or their derivatives, a single mismatch at position 17 resulted in a substantial (8.3- to 64-fold) reduction of k_{slice}, which indicated that a base-paired match at position 17 was necessary for rapid slicing in these sequence contexts (Figure 5A). Therefore, in contrast to the case of position 7, the preference for an A:U or U:A pair at position 17 does not seem to stem from a preference for a weak pair. We suspect it arises instead from a sequence-specific preference mediated through protein-RNA interactions.

The requirement for pairing at position 17 seemed at odds with the reports that pairing beyond position 16 is dispensable for efficient slicing.[39,42] Alternatively, because

the previous studies had examined pairing requirements for only two miRNAs (let-7a and miR-21), pairing beyond position 16 might be dispensable for efficient slicing guided by only a subset of RNA sequences. To investigate this possibility, we measured the k_{slice} values of target RNAs with complementarity up to only position 16 (hereafter referred to as 16-bp targets) for 12 different guide RNAs, and compared them to the

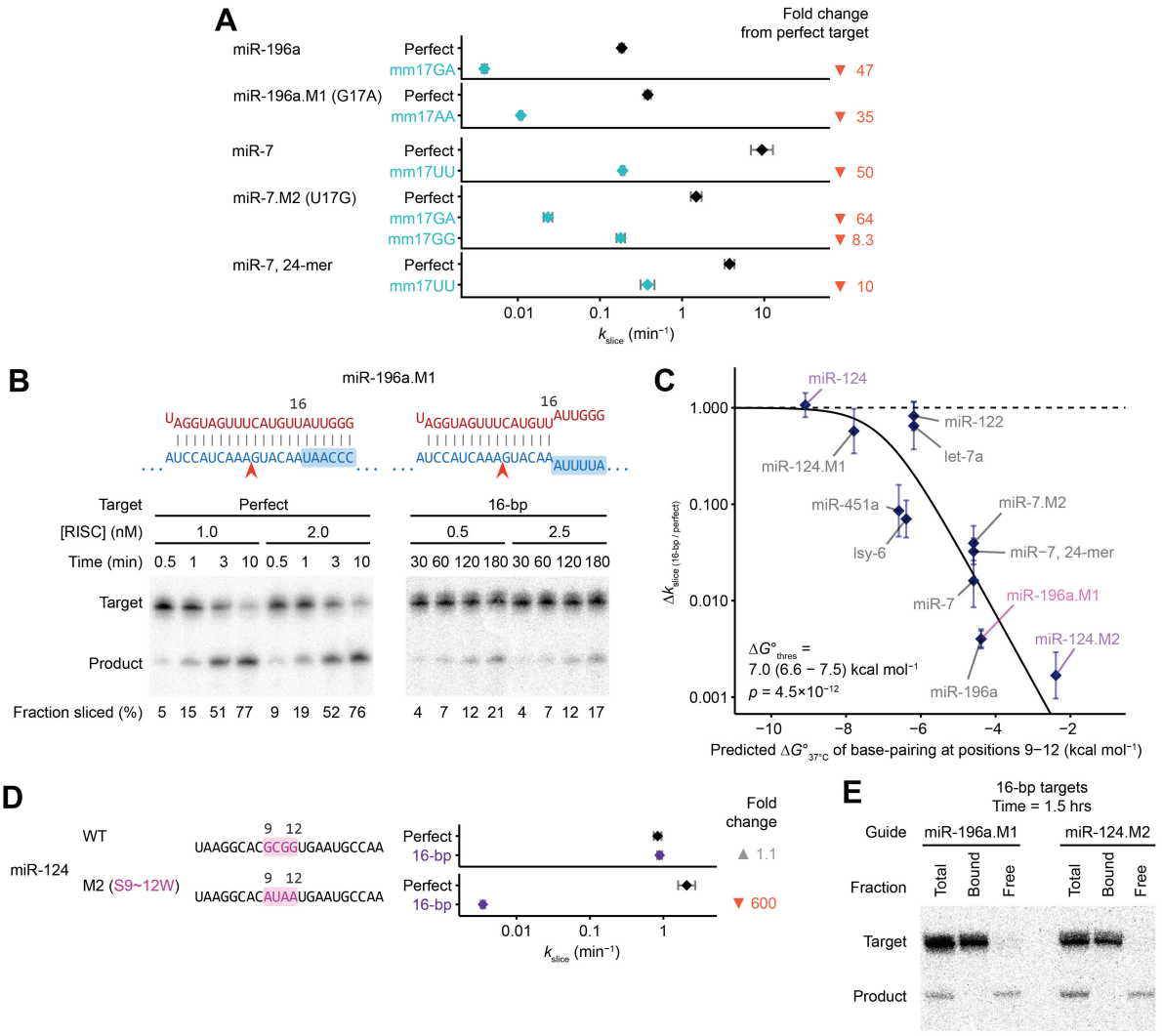

Figure 5. Slicing partially complementary targets with mismatches near the 3′-end is associated with strong predicted central pairing

(A) The importance of pairing to position 17. Measured are k_{slice} values for perfectly paired targets (black) or targets harboring a mismatch at position 17 (cyan); otherwise, as in Figure 2C.

(B) The importance of pairing to positions 17–22. Shown are schematics and representative results for miR-196a.M1-directed slicing of its perfectly complementary and 16-bp targets. Nucleotides in the target that were changed to introduce terminal mismatches are highlighted in blue; otherwise, as in Figure 2B.

(C) Relationship between the fold change in k_{slice} observed for 16-bp targets and the predicted base-pairing energy at positions 9−12. Error bars indicate 95% CIs based on propagated uncertainty from

model-fitting for the two k_{slice} values under consideration. The curve shows the nonlinear least-squares best fit of a thermodynamic equation involving one fitted parameter ($\Delta G°_{thres}$); its fitted value is shown with its 95% CI and *p* value as calculated by the *t*-test.
(D) Mutational evidence confirming the relationship between the strength of central pairing and the importance of pairing to positions 17–22. Measured are k_{slice} values for perfectly complementary or 16-bp targets, for miR-124 and its mutant (miR-124.M2), in which the central G/C nucleotides (S) of miR-124 were replaced with A/U nucleotides (W). Substituted positions are highlighted in the schematic, and values from 16-bp targets are plotted in purple; otherwise, as in (A).
(E) Evidence that slowly sliced 16-bp targets are nonetheless fully bound. Shown are results of slicing assays with 16-bp targets, in which the RISC-bound and free RNA species were separated by filter-binding after 1.5 hours of incubation. RISC was at 1 nM and the target was initially at 0.05 nM.

k_{slice} values of perfectly complementary targets. Although k_{slice} was only minimally reduced for some guide RNAs, k_{slice} was reduced by >100-fold for others, with the slowest measured half-life of slicing reaching 16 h (95% CI, 15 − 17 h) (Figures 5B and 5C). This variation was strongly correlated with the predicted pairing free energy of the central region of the guide−target RNA duplex (the four pairs closest to the cleavage site) (Figure 5C), which is proposed to be the final region of the target–guide duplex to form prior to slicing.[2] For example, the miR-124 complex, which had very stable predicted central pairing, imparted by a GCGG at positions 9−12 of miR-124, had a k_{slice} value for its 16-bp target that was indistinguishable from that for its perfectly complementary target. In contrast, the miR-196a.M1 complex, which had UUCA at positions 9−12, sliced its 16-bp target 250-fold slower than it sliced its perfectly complementary target (Figure 5B). To test this idea, we changed positions 9−12 of miR-124 to AUAA to generate miR-124.M2, which had the least stable predicted central pairing among the miRNAs tested. This change imparted a 600-fold drop in the k_{slice} value when slicing the 16-bp target, to a slicing half-life of 3.3 h (95% CI, 3.1 – 3.6 h) (Figures 5C and 5D).

To confirm that this drop represented a change in k_{slice} and not target association, we used filter-binding to monitor association at pre-steady-state timepoints. For both miR-196a.M1 and miR-124.M2, essentially all of the unsliced 16-bp target was bound by RISC at these early time points, confirming that the slow reaction rate was due to slow slicing (Figure 5E).

We conclude that base-pairing beyond position 16 is dispensable for efficient slicing only when the central region has high predicted pairing stability. This pairing energy is likely required to release the 3′-end of the guide from the AGO2 PAZ domain without the help of additional 3′-base-pairing, thereby allowing the RISC−target complex to adopt a slicing-competent conformation.[30] Thus, the GC-content at position 9−12

constitutes an additional sequence determinant for efficient AGO2-catalyzed slicing of partially complementary target RNAs.

The kinetics, not the thermodynamics, of conformational change dictate k_{slice}

Next, we examined how the effects of guide-RNA sequences on slicing perfectly complementary targets might be biophysically mediated through their influence on the conformational changes required to reach the slicing-competent state. To account for the energetic challenges of conformational changes needed to achieve the slicing-competent state (Figure S1A), k_{slice} can be modeled as a combination of the conformational changes (k_{con+} and k_{con-}) and the subsequent chemical step of phosphodiester bond hydrolysis (k_c), in which the former presumably varies between different sequence and base-pairing contexts (Figure 6A). The prevailing model of AGO2 slicing proposes that the conformational changes required to achieve the slicing-competent state are rapid but thermodynamically unfavorable, such that the low occupancy of the slicing-competent state at equilibrium (determined by K_{con}) limits k_{slice}.[36,63,64] An alternative to this thermodynamic model is the kinetic model, in which the conformational changes are slow due to a high energetic barrier, such that a slower, rate-limiting k_{con+} imparts a slower k_{slice} (Figure 6A; Figure S7A).

To examine the conformational impact of guide-RNA sequences in the context of these two models, we used hydroxyl-radical footprinting to assess RISC conformations. Hydroxyl radicals can cleave the RNA backbone at solvent-exposed positions, creating a banding pattern on an electrophoretic gel that reports on the reactivity, and thus the solvent accessibility, of each backbone position in a radiolabeled RNA.[65] The published structure models indicate that, as the RISC−target complex reaches the slicing-competent state, solvent accessibility of the miRNA backbone undergoes characteristic changes.[35,36] Prior to binding and following initial binding, the backbone is largely protected, except near position 18, where it loops around the PAZ domain; in contrast, in the slicing-competent state, the miRNA backbone becomes solvent-exposed near positions 9−11 and after position 18, aligning with the helical periodicity of a continuous guide−target duplex (Figure 6B). We thus reasoned that using hydroxyl-radical footprinting to measure the solvent accessibility of the guide backbone could reveal the rate and degree to which an RISC−target complex adopts the slicing-competent state.

To prevent the complex from slicing the target during the course of the experiment, we used a version of AGO2 that carried a point substitution at the active site ($AGO2^{D669A}$) (Figures 6B and 6C). We tested four different miRNAs, which spanned the dynamic range of k_{slice} values for perfectly complementary targets (Figures 6D, 6E,

and 2D). Each miRNA was radiolabeled, purified in association with AGO2^{D669A}, and incubated with excess target RNA for 30 min before adding Fenton's reagent, which generated hydroxyl radicals to initiate cleavage at exposed positions (Figure 6C). For each miRNA, the experiment was performed with either no target RNA or with one of several different target RNAs, each with different pairing potential to the miRNA (Figure S7B).

When AGO2^{D669A}–miRNA complexes were not engaged with target RNAs, the miRNA backbones generally had low reactivity across their lengths, with a moderate peak near position 18, as expected (Figures 6D and 6E; Figure S7C). When the complexes engaged with either targets that paired only to the seed or targets with five additional supplementary pairs, the reactivity profiles were largely unchanged (Figures S7C and S7D), in agreement with the crystal structures of these states.[35,59] When the complexes were engaged with targets with seed and extensive 3′ base-pairing, the miRNA backbones had increased solvent accessibility from around position 12 to the 3′ end, again in agreement with the structures (Figures S7C and S7E).[60]

When the complexes engaged with perfectly complementary target RNAs, the reactivity profiles closely matched those expected for the slicing-competent state, with strong peaks near positions 9−11 and after position 18 (Figures 6D and 6E; Figure S7C). Importantly, the profiles observed for each of the four miRNAs were similar, despite their very different k_{slice} values, an observation in stark contrast to the expectation of the thermodynamic model, which predicts that steady-state occupancy of the slicing-competent state is lower for guide RNAs with slower k_{slice}. In fact, across the four miRNAs, we found no significant differences in the heights of the central-region reactivity peaks diagnostic of the slicing-competent state, implying no significant differences in the equilibrium occupancy of the catalytic conformation for fast- and slow-slicing guides.

Having acquired evidence disfavoring the thermodynamic model, we modified the incubation protocol to investigate the validity of the kinetic model. Rather than probing the conformational states after incubating the complex with a perfectly complementary target for 30 min, we probed after incubating for only 1 min. After this short incubation, the two miRNAs with faster k_{slice} values had reactivity profiles diagnostic of the slicing-competent state, with the characteristic peaks in the central region, whereas the two guide RNAs with slower k_{slice} had reactivity profiles resembling the baseline of the no-target or initial-binding states (Figure 6E). Using the peak height at positions 9−11 as a proxy for the fractional occupancy of the slicing-competent state, we found a near-1:1 correspondence with the fraction of target RNA that would be sliced at 1 min when using the wildtype protein (Figure 6F). These results indicated that the kinetics of slicing

are limited kinetically, not thermodynamically, by the conformational change of the RISC−target ternary complex, such that guide-RNA sequence determinants enhance the slicing kinetics of perfectly complementary targets by promoting a faster conformational change to the slicing-competent state.

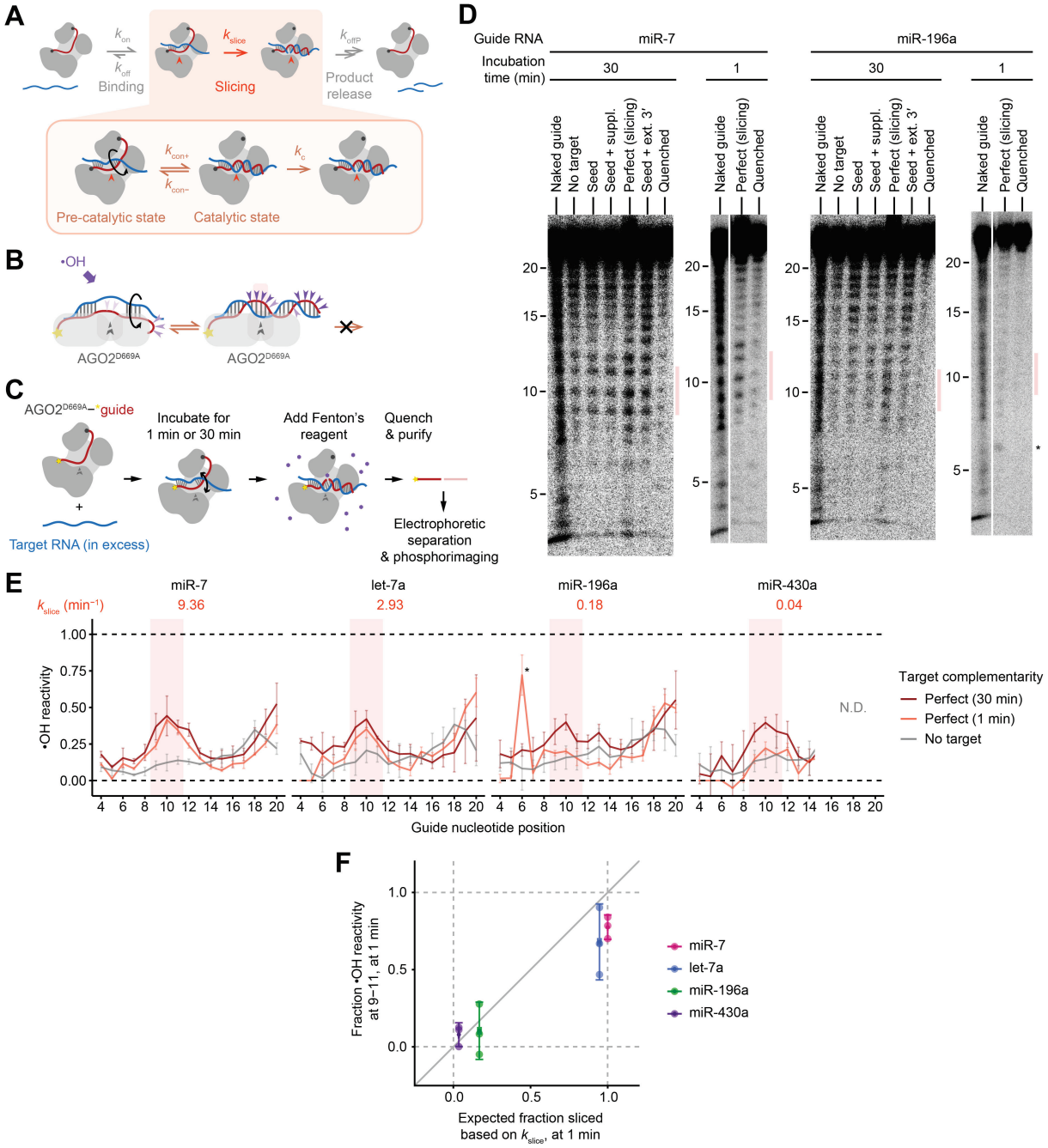

Figure 6. RISC conformational change kinetically limits k_{slice}

(A) Expanded kinetic scheme illustrating how conformational dynamics of the RISC−target complex could contribute to slicing kinetics; otherwise, as in Figure 1C.

(B) Schematic of changes in solvent accessibility of the guide upon conformational change to the catalytic state, as probed by hydroxyl radicals. Nucleotides shielded from solvent by AGO2 are shown in gray. Exposed guide backbone positions predicted to be readily cleaved by hydroxyl radicals are indicated with purple carets. The D669A mutation of AGO2, which prevents slicing and thus release of sliced product fragments, is represented as a broken gray caret at the active site. The site of ^{32}P radiolabel in the guide is indicated with a yellow star. Otherwise, colors are as in Figure 1A.
(C) Schematic of the hydroxyl-radical footprinting experiment. Colors are as in (A) and (B).
(D) Representative results from hydroxyl-radical footprinting experiment of AGO2^{D669A}–miR-7 or AGO2^{D669A}–miR-196a engaged with targets with different pairing potential. Samples with naked guides or quenched reagents provided the maximum and baseline signal intensities, respectively. Positions 9−11 are highlighted with orange bars on the right. An outlier observed at position 6 for miR-196a after one minute of incubation with a perfect target is indicated with an asterisk.
(E) Evidence that the slicing state is kinetically limited. Plotted are footprinting reactivity values observed when RISC was bound to either no targets or slicing targets. Reactivity values were normalized to the naked-guide or quenched-reagents samples (dashed lines). Position 21 was not confidently separated from the full-length band, and positions 1−3 were not resolved from the salt front. Positions 15−20 of miR-430a could not be confidently quantified (N.D.) due to minor trimmed guide isoforms in the input (Figure S7C). An outlier position for miR-196a is indicated with an asterisk. Error bars indicate 95% CIs based on four replicates for miR-196a bound to no targets or to slicing targets for 30 min, and three replicates for all other conditions. Positions 9−11 are shaded.
(F) Correspondence between fractional occupancy of catalytic state observed at one minute and the expected fraction of sliced target based on k_{slice}. The fractional occupancy was calculated as the reactivity at positions 9−11 relative to that at steady-state. Three replicates were performed for each guide. Error bars along both axes indicate 95% CIs for the mean relative reactivity.
See also Figure S7.

DISCUSSION

The discovery of significant variation in slicing kinetics when AGO2 is loaded with different guides emphasizes that different miRNAs or siRNAs can have substantially different biochemical behaviors and preferences. Some of the biochemical properties of AGO2, such as the preference for U at position 1 of the guide[53,66] and the site of slicing residing between nucleotides paired to positions 10−11,[67] are likely universal and generalizable. Other properties, however, such as the relative strengths of different site types,[44] the positional preferences of additional 3′ base-pairing,[68] the kinetics of slicing, and the tolerance for mismatches for slicing, must be examined on a guide-by-guide basis. Predictions of the biochemical outcome of a RISC-binding site must consider both the properties of both AGO2 and the specific guide-RNA sequence of interest.

Guide-specific properties were illustrated most emphatically by the 600-fold range in 3′-mismatch tolerance. The notion that slicing is insensitive to (or even favored by) mismatches beyond position 16 of the guide RNA, which comes from analyses of just two guide RNA sequences,[39,42] has led to the idea that RISC bound a 16-nt-bp target provides the most appropriate structure model for the slicing configuration.[35,36]

The fact that slicing kinetics can vary widely for target sites with identical site architectures reveals new potential modes of regulation for the efficacy of AGO2-mediated knockdown. First, although most miRNA hairpins in the human transcriptome contain mismatches to allow AGO to eject the passenger strand without slicing, at least two endogenous miRNAs in humans require slicing for their processing and maturation in AGO2.[20–22] Most synthetic siRNA duplexes designed for RNAi, as well as endogenous-siRNA duplexes in some species other than human, also feature complete complementarity and presumably require slicing for the removal of the passenger strand.[24–26] The maturation of these miRNAs and siRNAs could be adjusted based on the sequence determinants of slicing, leading to an altered effective concentration of the enzyme complex in cells. Second, as the dynamic ranges of all kinetic parameters (k_{on}, k_{slice}, and k_{offP}) along the catalytic mechanism of AGO2 overlap each other almost entirely (Figure S5E), any of these kinetic steps can become rate-limiting, and therefore influence the functional output of RNAi for a given guide–target pair in cells. For guides with low k_{slice} values, the time required for slicing can represent a non-trivial time delay for the degradation of most mRNAs, given their typical half-lives in human cells.[69–71] The range of k_{slice} values also spans the typical kinetics of other cellular functions, such as translation, although increasing the number of ribosomes translocating through the target site did not appear to influence reporter repression.

One explanation our inability to detect an effect of ribosomes centers on the possibility that the very strong affinity of RISC for perfectly complementary sites[34] (K_D << 10 pM) might cause the ribosome to stall before displacing the RISC[72] and thereby increase the propensity of ribosomes to collide with each other. Such collisions might trigger the no-go decay pathway, resulting in the degradation of the mRNA,[73] as observed for antisense oligonucleotides paired to coding sequences,[74] which would enhance reporter repression. Thus, inducing translation of the reporter might have had two offsetting effects: increased ribosome-mediated displacement of RISC, causing reduced RISC-catalyzed reporter slicing, and increased ribosome collisions, causing increased reporter degradation through no-go decay.

When AGO2 loaded with a slow-slicing guide is bound to a slicing target site, other parallel functional pathways might have the opportunity to occur. As AGO2's tryptophan-binding pockets are not altered during conformational changes,[75] a bound RISC is expected to recruit TNRC6 and associated factors, leading to the deadenylation and decapping of the target transcript. In addition, perfectly complementary sites might also be able to trigger the degradation of the bound RISC.[76,77] The probability partition between the possible pathways with different functional outcomes would depend on their relative kinetic competition and perhaps the competition of associated biochemical

factors. Better understanding of the relative efficiencies of these parallel functional pathways, with consideration of the sequence determinants of slicing rates, would allow more confident prediction of the main mechanistic pathway and the ultimate functional outcome for each possible target site in the transcriptome.

The preference for a purine at position 10 of the guide was the strongest sequence determinant of k_{slice} that we found, and was also the strongest sequence-specific feature found in siRNA functional screens.[51] The mechanistic basis for its effect on slicing kinetics, however, remains unknown. Its proximity to the site of RNA cleavage suggests that it either forms favorable interactions with the central chamber of AGO2 during the conformational transition to the slicing configuration or allows the optimal configuration of the active site to be more readily adopted. With respect to the sequence determinant at position 17, structure models suggest that this base pair makes minor-groove contact with the N domain of AGO2,[36] a mode of contact known to distinguish between A:U/U:A and G:C/C:G pairs.[78] Given the pivotal role of N domain in regulating slicing,[79,80] this contact might explain the strong influence of position 17 on k_{slice}. Finally, as the sequence determinant at position 7 lies within the seed region, it may serve additional roles beyond its effect on slicing. Examining structure models suggest that the local helical distortion found may be caused by the interaction with helix-7 of AGO2, which has previously been shown to modulate the strength of seed-site affinity.[33] Future structural and biochemical studies would allow a deeper understanding of the molecular interactions responsible for the sequence preferences found.

The observation that flexible or mismatched pairs at position 6–7 of the guide-RNA seed promote slicing illustrates that imperfections in the seed match can be favored in this context in which extensive pairing to the remainder of the guide RNA are more than sufficient for target binding. Of course, in the context of typical miRNA–target interactions, which are primarily mediated by seed pairing, these imperfections in the seed match would greatly reduce binding and repression.[44,61]

Two aspects of our results are particularly relevant for the design of new RNAi-based therapeutics. First, contrary to previous models, the limiting factor for slicing perfectly complementary targets is the rate of conformational change, rather than its thermodynamics. Accordingly, the most relevant transition state for slicing kinetics is the most energetically unfavorable point of the conformational change, immediately before the formation of the fully paired duplex and proper positioning of the active site (Figure S7A). Thus, the design of chemically modified siRNAs would be the most productive when directed towards the stabilization of this transition state instead of the final catalytic conformation. Second, it has been proposed that siRNAs with complementarity that ends at position 16 would have enhanced performance.[39] Our

results indicate that this would be a viable strategy only for siRNAs with unusually strong pairing at their central region. On the other hand, designs involving weaker central pairing would increase specificity, avoiding potential off-target slicing at sites that have only partial complementarity.

METHODS

In vitro transcription of target RNAs

Single-stranded DNA templates (Table S2), each containing a T7 promoter sequence, were synthesized (IDT), purified on a 12% or 15% urea-polyacrylamide gel, and resuspended in water. Each template DNA was annealed with an oligonucleotide complementary to the T7 promoter sequence (Table S2), and then used in an in vitro transcription reaction containing 0.5 μM annealed DNA template, 5 mM ATP, 2 mM UTP, 5 mM CTP, 8 mM GTP, 5 mM DTT, 40 mM Tris pH 7.9, 2.5 mM spermidine, 26 mM $MgCl_2$, 0.01% (v./v.) Triton X-100, 5 mM DTT, SUPERase•In (1 U/μL, Invitrogen, AM2694), thermostable Inorganic Pyrophosphatase (0.0083 U/μL, New England Biolabs, M0296), and T7 RNA Polymerase (purified in-house). The reaction was incubated at 37°C for 3−4 h, before RQ1 DNase (0.037 U/μL, Promega, M6101) was added, followed by 30 min of incubation at 37°C. The final reaction mix was desalted using Micro Bio-Spin P-30 columns (Bio-Rad, 7326250), then denatured by incubating with 0.5X volume of gel-loading buffer (8 M urea, 25 mM EDTA, 0.025% [w./v.] xylene cyan, 0.025% [w./v.] bromophenol blue) or Gel Loading Buffer II (Invitrogen, AM8547) at 90°C for 1 min. The full-length RNA product was then purified on a 12% or 15% urea-polyacrylamide gel and resuspended in water.

Preparation of radiolabeled RNAs

Guide RNAs (Table S2) were synthesized with a 5′ monophosphate (IDT), purified on a 15% urea-polyacrylamide gel, and then resuspended in water. To radiolabel, guide RNAs were first dephosphorylated using shrimp alkaline phosphatase (rSAP, 0.05 U/μL; New England Biolabs, M0371) at 37 °C for 30 min, followed by heat-inactivation at 75°C for 5 min and desalting using Micro Bio-Spin P-6 columns (Bio-Rad, 7326221). Dephosphorylated guide RNAs were then radiolabeled using T4 Polynucleotide Kinase (0.33 U/μL, New England Biolabs, M0201) and 0.42 μM [γ-^{32}P] ATP (PerkinElmer, NEG035C001MC) at 37°C for 1.5 h, before a brief chase with 0.16 mM ATP at 37°C for 15 min, followed by desalting using Micro Bio-Spin P-6 columns and denaturation with gel-loading buffer or Gel Loading Buffer II. Radiolabeled guide RNAs were purified on a 15% urea-polyacrylamide gel, and then resuspended in water.

Short target RNAs, containing a seed (7mer-m8 or 8mer)-only binding site for titration quantification (Table S2), were synthesized (IDT), purified on a 15% urea-polyacrylamide gel, and then resuspended in water. These RNAs were then radiolabeled with T4 Polynucleotide Kinase and 2.5 μM [γ-^{32}P] ATP at 37°C for 1.5 h, followed by the chase and purification described for radiolabeled guide RNAs.

In vitro-transcribed target RNAs (Table S2) were radiolabeled with ^{32}P at either a 5′ monophosphate or a 7-methylguanylate cap. The identity of target 5′ chemistry had no detectable impact on our biochemical assays. When labeling at a 5′ monophosphate, RNAs were first dephosphorylated using Quick CIP (0.1 U/μL, New England Biolabs, M0525) at 37°C for 15 min, followed by heat-inactivation at 80°C for 3 min. Dephosphorylated RNAs were then radiolabeled using T4 Polynucleotide Kinase (0.67 U/μL) and 0.84 μM [γ-^{32}P] ATP, in CutSmart buffer (New England Biolabs) supplemented with 5 mM DTT, at 37°C for 1.5 h, before a brief chase with 0.32 mM ATP at 37°C for 15 min. When labeling at a 7-methylguanylate cap, RNAs were capped using the *Vaccinia* capping system (New England Biolabs, M2080) with [α-^{32}P] GTP (PerkinElmer, NEG006H250UC), according to manufacturer's instructions. Reactions from either labeling method were desalted using Micro Bio-Spin P-30 columns, denatured with gel-loading buffer or Gel Loading Buffer II, purified on a 12% or 15% urea-polyacrylamide gel, and then resuspended in water.

Purification of RISCs

5′-phosphorylated guide and passenger RNAs (Table S2) were synthesized (IDT), purified on a 15% urea-polyacrylamide gel, and then resuspended in water. Passenger RNAs were designed to create mismatches in the seed and 2-nt 3′-overhangs on both ends of the guide−passenger RNA duplexes, in order to direct the correct strand selection by AGO2.[85] Guide−passenger RNA duplexes were assembled using 1 μM each of guide and passenger RNAs, with 1−10% ^{32}P-radiolabeled guide RNA, in annealing buffer (60 mM Tris-HCl pH 7.5, 200 mM NaCl, and 2 mM EDTA). RNAs were annealed by heating to 90°C and then slowly cooling over 1.5 h to 30°C, before being chilled on ice and stored at −20°C.

Each RISC was assembled in lysate containing tagged AGO2 protein and then purified by oligo-affinity capture and competitive elution.[45] Lysates containing AGO2 proteins, N-terminally tagged with a 3xFLAG sequence, were generated as follows: HEK293FT cells were cultured in DMEM (VWR, 45000-304) supplemented with 10% FBS (Takara Bio, 631367), at 37 °C in 0.5% CO_2, and co-transfected at ~80% confluency with the pcDNA3.3−3xFLAG−AGO2[44] (Addgene plasmid #136687) and

pMaxGFP (Lonza) plasmids at 4:1 ratio (by mass) using Lipofectamine 2000 (Invitrogen, 11668019) in Opti-MEM (Gibco, 51985091), according to manufacturers' instructions. After 24 h, cells were harvested and lysed in hypotonic buffer (10 mM HEPES pH 7.4, 10 mM KOAc, 1.5 mM $Mg(OAc)_2$, 0.5 mM DTT, with cOmplete Mini EDTA-free Protease Inhibitor Cocktail [1 tablet per 10 mL, Roche, 11836170001]) by passing through a 23G × 1 inch needle 30 times. Cell lysate was clarified by centrifugation at 2,000*g* at 4°C for 10 min four times, then once for 30 min. The supernatant of this hypotonic lysate was re-equilibrated by adding 11% volume of re-equilibration buffer (300 mM HEPES pH 7.4, 1.4 M KOAc, 30 mM $Mg(OAc)_2$, with 1 tablet per 10 mL cOmplete Mini EDTA-free Protease Inhibitor Cocktail), before further clarification by centrifugation at 100,000*g* at 4°C for 20 min. 20% lysate-volume of 80% (v./v.) glycerol was added before flash-freezing in liquid nitrogen in aliquots of 600 µL for storage at −150°C.

To assemble each RISC, 300−600 µL of cell lysate was incubated for 2 h at 25°C with 11% lysate-volume of assembled guide−passenger duplex, with the final concentration of the duplex at 100 nM. Loaded lysate was centrifuged at 21,000*g* at 4°C for 10 min, and the supernatant was incubated with 150 µL of a slurry of Dynabeads MyOne Streptavidin C1 (Invitrogen, 65002) pre-bound to 75 pmol of capture oligonucleotide (Table S2), at 25°C with shaking at 1,300 rpm for 1.25 h. These pre-bound streptavidin beads were prepared by equilibrating the beads according to manufacturer's instructions, followed by incubation with 75 pmol of 3′-end biotinylated, fully 2′-*O*-methylated oligonucleotides (IDT) containing a seed-only 8mer-site for the guide RNA (Table S2), at 25°C with shaking at 1,300 rpm for 30 min. The beads were then washed in 300 µL equilibration buffer (18 mM HEPES pH 7.4, 100 mM KOAc, 1 mM $Mg(OAc)_2$, 0.01% [v./v.] IGEPAL CA-630 [Sigma-Aldrich, I3021], 0.1 mg/mL BSA [New England Biolabs, B9000], and 0.01 mg/mL yeast tRNA [Life Technologies, AM7119]) before use. After incubation with the loaded lysate, the beads were washed five times with 200 µL equilibration buffer, and five times with 200 µL capture-wash buffer (18 mM HEPES pH 7.4, 2 M KOAc, 1 mM $Mg(OAc)_2$, 0.01% [v./v.] IGEPAL CA-630, 0.1 mg/mL BSA, and 0.01 mg/mL yeast tRNA). Washed beads were incubated with 150 µL of competitor elution solution (0.75 µM of 3′-biotinylated DNA competitor oligonucleotides [IDT] complementary to the capture oligonucleotides (Table S2), 18 mM HEPES pH 7.4, 1 M KOAc, 1 mM $Mg(OAc)_2$, 0.01% [v./v.] IGEPAL CA-630, 0.1 mg/mL BSA, and 0.01 mg/mL yeast tRNA) at 25 °C with shaking at 1,300 rpm for 2 h. Purifications of AGO2−miR-451a and AGO2–miR-451a.M1 complexes used competitor oligonucleotides without 3′-biotinylation, with negligible difference in performance. The eluate was then incubated with 20 µL of an anti-FLAG M2 magnetic beads slurry

(Millipore, M8823), pre-equilibrated in equilibration buffer according to manufacturer's instructions, at 25°C with shaking at 1,100 rpm for 2 h. The beads were washed three times with 200 µL of equilibration buffer, and three times with 500 µL of equilibration buffer, before incubation in 60 µL 3xFLAG elution solution (146 ng/µL of 3xFLAG peptide [Sigma-Aldrich, F4799] in 0.97X equilibration buffer) at 25°C with shaking at 1,100 rpm for 1 h. The eluate was supplemented with glycerol and DTT to a final storage buffer condition of 13.0 mM HEPES pH 7.4, 72.3 mM KOAc, 0.723 mM $Mg(OAc)_2$, 5 mM DTT, 0.0723 mg/mL BSA, 0.00723 mg/mL yeast tRNA, 0.00723% (v./v.) IGEPAL CA-630, and 20% (v./v.) glycerol, before flash-freezing in liquid nitrogen for storage at −80°C.

To produce complexes with mutant AGO2 proteins, including $AGO2^{D669A}$, $AGO2^{S387A}$, and $AGO2^{S387D}$, the corresponding plasmids were generated by site-directed mutagenesis of the pcDNA3.3−3xFLAG−AGO2 plasmid, by PCR (Table S2) using KAPA HiFi HotStart Ready Mix (Roche, 07958935001). Plasmid sequences were confirmed by Sanger sequencing.

$AGO2^{D669A}$−guide complexes used for hydroxyl-radical footprinting were purified in a similar manner but without inclusion of glycerol in the final storage buffer (17.4 mM HEPES pH 7.4, 96.6 mM KOAc, 0.966 mM $Mg(OAc)_2$, 5 mM DTT, 0.0966 mg/mL BSA, 0.00966 mg/mL yeast tRNA, and 0.00966% [v./v.] IGEPAL CA-630). Small aliquots were flash-frozen in liquid nitrogen for storage at −80 °C.

Quantification of purified RISCs

Each purified RISC was first run on a 15% urea-polyacrylamide gel alongside the guide−passenger duplex used for its purification. Gels were frozen at −20 °C while exposing a phosphorimager plate, and radioactivity was then imaged using Typhoon FLA 7000 (GE Healthcare), Typhoon FLA 9500 (GE Healthcare), or Amersham Typhoon (Cytiva) phosphorimager. Images were quantified using either the Multi Gauge (Fujifilm) or ImageQuant TL (Cytiva) software. Radioactivity of the guide in the purified RISC relative to that in the duplex (for which the concentration was known) provided an estimate for the concentration of the purified complex.

Concentrations of purified complexes were then more accurately determined using a titration assay. A dilution series of RISC concentrations that were designed to not exceed 1 nM, were each incubated with 1 nM of radiolabeled oligonucleotides harboring a single canonical 7mer-m8 or 8mer binding site for the corresponding guide RNA. Binding reactions were incubated at 37°C for 1 h, in a final binding reaction buffer of 15.5 mM HEPES pH 7.4, 86.2 mM KOAc, 0.862 mM $Mg(OAc)_2$, 5 mM DTT, 0.05

mg/mL BSA, 0.005 mg/mL yeast tRNA, and 10% (v./v.) glycerol. To carry out filter-binding experiments, nitrocellulose (Amersham Protran, 0.45 µm pores; Cytiva, 10600062) and nylon (Amersham Hybond-XL; Fisher Scientific, 45001147) membrane filters were cut into discs of 0.5 inch diameter and equilibrated at 25°C for at least 20 min in filter-binding buffer (18 mM HEPES pH 7.4, 100 mM KOAc, 1 mM $Mg(OAc)_2$). Each nitrocellulose disc was stacked on top of a nylon disc, then placed on a circular pedestal mounted on a Visiprep SPE Vacuum Manifold (Supelco, 57250-U), set at approximately −20 kPa. 10 µL of reaction was applied to stacked filter membrane discs, followed by 100 µL of ice-cold filter-binding wash buffer (18 mM HEPES pH 7.4, 100 mM KOAc, 1 mM $Mg(OAc)_2$, 5 mM DTT). Filter membrane discs were separated, air-dried, then imaged by phosphorimaging and quantified using either the Multi Gauge or ImageQuant TL software.

Fractions of target RNA bound across reactions were used to quantify stock concentration of RISCs, assuming a 1:1 stoichiometric ratio of RISC and bound target and K_D of the binding reaction far below the total target concentration. Datasets that did not approach target saturation (≤ 60% bound) were fit by linear regression in R (lm) to the following equation:

$$F_{bound} = \frac{[\text{stock}] \cdot DF}{[\text{target}_T]} + yint$$

where F_{bound} represents fraction of target bound, $[\text{target}_T]$ represents concentration of total target oligonucleotide (1 nM), [stock] represents stock concentration of RISC, *DF* represents the dilution factor, and *yint* represents the *y*-intercept, which was near zero for all datasets.

Datasets approaching saturation were instead fit to a quadratic equation by nonlinear least-squares regression in R using the Levenberg-Marquardt algorithm (nlsLM from the R package minpack.lm):

$$F_{bound} = \frac{([\text{stock}] \cdot DF + [\text{target}_T] + K_D) - \sqrt{([\text{stock}] \cdot DF + [\text{target}_T] + K_D)^2 - 4 \cdot [\text{stock}] \cdot DF \cdot [\text{target}_T]}}{2 \cdot [\text{target}_T]} \cdot (1 - yint) + yint$$

where K_D additionally represents the dissociation constant for the affinity between RISC and the seed-match target. [stock] was initialized at 30,000 pM and limited to the numerical range (0, 10^6); *yint* was initialized at 0.1 and limited to the numerical range (0, 1); K_D was initialized at 10^2 pM, limited to the numerical range (10^{-2}, 10^4), and fit in log-transformed space. For lsy-6, the nonlinear least-squares regression did not produce a

confident estimation of stock concentration ($p > 0.05$), and thus the results from a linear regression of data points before saturation were used instead.

In vitro slicing assays

Target RNAs for slicing assays were designed with a perfectly or partially complementary slicing site, flanked by poly(AAC) or poly(UUC) sequences designed to reduce secondary structure. Single-turnover assays were conducted with 0.02−0.10 nM of radiolabeled target RNA and a dilution series of RISC concentrations (at 0.09−33 nM and 4.5−660-fold excess over the target across all assays). Target RNA was preincubated in slicing-reaction buffer (18 mM HEPES pH 7.4, 100 mM KOAc, 1 mM $Mg(OAc)_2$, 5 mM DTT, 0.01% [v./v.] IGEPAL CA-630) at 37°C for 1.5 min, while the RISC was preincubated in storage buffer at 37°C for 0.5 min, before an equal volume of preincubated RISC was added to preincubated target RNA in buffer, to a final reaction condition of 15.5 mM HEPES pH 7.4, 86.2 mM KOAc, 0.862 mM $Mg(OAc)_2$, 5 mM DTT, 0.05 mg/mL BSA, 0.005 mg/mL yeast tRNA, and 10% (v./v.) glycerol. Reactions were incubated at 37°C. At select time points, aliquots of the reaction were quenched by mixing rapidly with gel-loading buffer or Gel Loading Buffer II on ice. Quenched reaction aliquots were denatured at 90°C for 1 min, and then run on a 15% urea-polyacrylamide gel. Gels were frozen at −20°C while exposing a phosphorimager plate, and radioactivity was imaged using a phosphorimager, then quantified.

Multiple-turnover assays were conducted with 4 nM radiolabeled target and ~0.25 nM RISC. Conditions for preincubation, reaction, and quenching, and methods of phosphorimaging and quantification, were otherwise the same as those of single-turnover assays.

Model-fitting of single-turnover slicing kinetics

Guesses were first determined for each dataset. k_{on} was initialized at 1 nM^{-1} s^{-1} for datasets with substantial contribution from slow association kinetics, and 10 nM^{-1} s^{-1} for datasets without. Datasets were defined to have substantial contribution from slow association kinetics if deviation in mean fraction of target sliced across different RISC concentrations was more than 0.15 at any time point. k_{slice} was initialized at 0.0167 s^{-1}, k_{phase2} at 3.33×10^{-6} s^{-1}, and F_a at 0.95 × the highest fraction of target sliced measured in the dataset. These were used to generate guesses by nonlinear least-squares regression in R to an approximation equation. Datasets were fit using the Levenberg-Marquardt algorithm (nlsLM), for no more than 50 iterations, to the following equation, assuming pseudo-steady-state of enzyme-substrate complex concentration:

$$F_{sliced} = F_a \cdot \left(1 - e^{-\frac{1}{\frac{1}{k_{on}\cdot[E_T]}+\frac{1}{k_{slice}}}\cdot t}\right) + (1 - F_a) \cdot (1 - e^{-k_{phase2}\cdot t})$$

where F_{sliced} represents fraction of target sliced, t represents time in s, k_{on} represents the association rate constant in $nM^{-1}\ s^{-1}$, $[E_T]$ represents the total concentration of RISC in nM, k_{slice} represents the slicing rate constant in s^{-1}, k_{phase2} represents the slow second-phase slicing rate constant in s^{-1}, and F_a represents the height of the first phase. k_{on} was limited to the numerical range (10^{-6}, 1), where 1 $nM^{-1}\ s^{-1}$ was the diffusion limit. k_{slice} was limited to the numerical range (10^{-6}, 1). k_{phase2} was limited to the numerical range (1.67×10^{-6}, 1.67×10^{-4}), where $1.67 \times 10^{-6}\ s^{-1}$ was the approximate detection limit based on the longest time points tested. F_a was limited to the numerical range (0.3, 0.999). If the nonlinear least-squares regression failed, the initial values were used with F_a adjusted to 0.85. For datasets with slow association kinetics, the fitted value of F_a was adjusted by a factor of 0.9 to account for overestimation of the plateau by the pseudo-steady-state approximation model.

These guesses were then used as initial values to fit the dataset to an ODE model to calculate accurate values:

$$\frac{d[P]}{dt} = k_{slice} \cdot [ES] + k_{phase2} \cdot [E'S]$$
$$\frac{d[ES]}{dt} = k_{on} \cdot [E][S] - k_{slice} \cdot [ES]$$
$$\frac{d[E]}{dt} = -k_{on} \cdot [E][S] + k_{slice} \cdot [ES]$$
$$\frac{d[E'S]}{dt} = k_{on} \cdot [E'][S] - k_{phase2} \cdot [E'S]$$
$$\frac{d[E']}{dt} = -k_{on} \cdot [E'][S] + k_{phase2} \cdot [E'S]$$
$$\frac{d[S]}{dt} = -k_{on} \cdot [E][S] - k_{on} \cdot [E'][S]$$

with

$$\begin{cases} [P] = 0 \\ [ES] = 0 \\ [E'S] = 0 \\ [E] = [E_T] \\ [E'] = [E'_T] \\ [S] = [S_T] \end{cases}, \text{when } t = 0$$

$$F_a = \frac{[E_T]}{[E_T] + [E'_T]} = \frac{[E_T]}{[E_{all}]}$$

such that, at each time point,

$$F_{sliced} = \frac{[P]}{[P] + [S] + [ES] + [E'S]}$$

where F_{sliced} represents fraction of target sliced, t represents time in s, $[E_T]$ represents total concentration of functionally intact RISC in nM, $[E'_T]$ represents total concentration of defective RISC in nM, $[E_{all}]$ represents total concentration of all RISCs, F_a represents the fraction of RISCs that is functionally intact, k_{on} represents the association rate constant in $nM^{-1}\ s^{-1}$, k_{slice} represents the slicing rate constant in s^{-1}, and k_{phase2} represents the defective slicing rate constant in s^{-1}.

Other biphasic ODE equations were also attempted to model the biphasic behavior as each of the following: (1) a small fraction of inactive RISCs binding to target RNAs but unable to slice, instead dissociating at k_{phase2}; (2) a small fraction of the enzyme-substrate complex adopting a slicing-incompetent conformation upon binding, dissociating at k_{phase2}; (3) a small fraction of the enzyme-substrate complex adopting a slicing-incompetent conformation upon binding, changing to a slicing-competent conformation at k_{phase2}; (4) a small fraction of the enzyme-substrate complex adopting a slicing-defective conformation upon binding, slicing at k_{phase2}; and (5) a small fraction of the enzyme-substrate complex undergoing unloading of the guide, leaving inactive naked guide RNA blocking the target RNA, dissociating at k_{phase2}. Although the fits for these rejected models were indistinguishable from those for the accepted model, these models were rejected in favor of the accepted model based on orthogonal experimental results (Figures S2D, S2F, and S5D). Importantly, the choice of models did not change any of our other interpretations or conclusions.

Fitting to the ODE model was carried out using the modFit function, with the Levenberg-Marquardt algorithm, from the FME package in R, for up to 200 iterations. At each iteration, reaction time curves were calculated for each pair of RISC and target concentration values using the Livermore solver for ordinary differential equations (LSODE) from the deSolve package (ode function) in R. Calculations were conducted using the backward differentiation formula with a full Jacobian matrix internally calculated by lsode (option mf = 22). Relative tolerance was set to 10^{-6}, while absolute tolerance was set to 10^{-10}. At each iteration, the cost function was defined to be the absolute deviation in fraction of target sliced between empirical and ODE-predicted values. Kinetic constants were fit in log-transformed space. k_{on} was limited to the numerical range (0, 1), where 1 $nM^{-1}\ s^{-1}$ was the diffusion limit. k_{slice} was limited to the numerical range (0, ∞). k_{phase2} was limited to the numerical range (1.67×10^{-6}, 3.33×10^{-3}). F_a was limited to the numerical range (0.3, 1.0). If k_{on} could not be confidently fit for fast-binding reactions due to trivial contribution from binding kinetics, model fitting

was repeated with k_{on} constrained to the diffusion limit at 1 nM^{-1} s^{-1}. If k_{phase2} could not be confidently fit due to insufficiently long time points to resolve the second phase, model fitting was repeated with k_{phase2} constrained to zero.

As RISC was in excess over the target, exact initial concentrations of target RNA had negligible impact on the reaction rates. While ODE model-fitting took into account exact initial concentrations of target RNA, reaction curves in figures were plotted with the initial target concentration at 0.02 nM for simplicity.

For some guides with rapid binding kinetics that did not contribute meaningfully to the reaction kinetics, reaction assays using other purifications of RISC as biological replicates were conducted at a single RISC concentration, and were fit with the binding kinetics constrained to the diffusion limit (1 nM^{-1} s^{-1}).

For some assays with mismatched targets (miR-124.M2, 16-bp target; miR-196a, 16-bp and mm17GA targets; miR-196a.M1, 16-bp and mm17AA targets), slicing kinetics were too slow for the plateau to be resolved even at very long time points, with no detectable contribution from association kinetics. Therefore, these datasets were instead fit by nonlinear least-squares regression in R using the Levenberg-Marquardt algorithm (nlsLM), for no more than 100 iterations, to the following equation:

$$F_{sliced} = F_a \cdot (1 - e^{-k_{slice} \cdot t})$$

where F_a was set to the fitted value from the same guide with its perfectly complementary target. k_{slice} was initialized at 1.67×10^{-4} s^{-1}, limited to the numerical range (0, ∞), and fit in log-transformed space.

Model-fitting of multiple-turnover slicing kinetics

Datasets were fit to the multiple-turnover ODE model, accounting for product release and re-binding:

$$\frac{d[P]}{dt} = k_{offP} \cdot [EP] + k_{offP} \cdot [E'P] - k_{on} \cdot [E][P] - k_{on} \cdot [E'][P]$$
$$\frac{d[EP]}{dt} = k_{slice} \cdot [ES] - k_{offP} \cdot [EP] + k_{on} \cdot [E][P]$$
$$\frac{d[ES]}{dt} = k_{on} \cdot [E][S] - k_{slice} \cdot [ES]$$
$$\frac{d[E]}{dt} = -k_{on} \cdot [E][S] + k_{offP} \cdot [EP] - k_{on} \cdot [E][P]$$
$$\frac{d[E'P]}{dt} = k_{phase2} \cdot [E'S] - k_{offP} \cdot [E'P] + k_{on} \cdot [E'][P]$$
$$\frac{d[E'S]}{dt} = k_{on} \cdot [E'][S] - k_{phase2} \cdot [E'S]$$

$$\frac{d[E']}{dt} = -k_{on} \cdot [E'][S] + k_{offP} \cdot [E'P] - k_{on} \cdot [E'][P]$$
$$\frac{d[S]}{dt} = -k_{on} \cdot [E][S] - k_{on} \cdot [E'][S]$$

with

$$\begin{cases} [P] = 0 \\ [EP] = 0 \\ [ES] = 0 \\ [E'P] = 0 \\ [E'S] = 0 \\ [E] = [E_T] \\ [E'] = [E'_T] \\ [S] = [S_T] \end{cases}, \text{when } t = 0$$

$$F_a = \frac{[E_T]}{[E_T] + [E'_T]} = \frac{[E_T]}{[E_{all}]}$$

such that, at each time point,

$$F_{sliced} = \frac{[P] + [EP] + [E'P]}{[P] + [EP] + [ES] + [E'P] + [E'S] + [S]} \cdot F_{max}$$

where, in addition to parameters defined in the single-turnover ODE equations, F_{max} represents the maximum plateau height of the fraction of target sliced, and k_{offP} represents the rate constant of product release in s^{-1}. Values of k_{on}, k_{slice}, k_{phase2}, and F_a were taken from single-turnover slicing assay results of the same RISC and target. k_{offP}, F_{max}, and $[E_{all}]$ were fit to the model, with k_{offP} being fit in log-transformed space, and $[E_{all}]$ being fit as a deviation from the experimentally intended concentration. For datasets with at least one measured fraction of target sliced exceeding 0.2 due to rapid catalytic kinetics, k_{offP} was initialized at 0.167 s^{-1} and limited to the numerical range (0, ∞), F_{max} was initialized at 0.95 and limited to the numerical range (0, 1), and $[E_{all}]$ was initialized at the experimentally intended concentration and limited to two-fold above or below this value. Fitted values of F_{max} were between 0.94 and 0.95 across five datasets. For datasets with all values of fraction of target sliced below 0.2, k_{offP} was initialized instead at 0.0167 s^{-1}, and F_{max} was not fit and instead constrained to 1.

Filter-binding for RISC binding kinetics

Filter-binding was conducted with target RNAs bearing a mismatch at position 10, or mismatches at positions 10−11 for lsy-6, to best mimic the binding of a perfectly complementary target without slicing. Filter membrane discs were prepared and preincubated in the same way as in filter-binding assays for RISC quantification. Target

RNA was preincubated in slicing-reaction buffer at 37°C for 1.5 min, while the RISC was preincubated in storage buffer at 37°C for 0.5 min, before an equal volume of RISC was added to the preincubated target RNA in buffer and mixed, with the final concentration of RISC at 0.5 or 1 nM, and the final concentration of target at 10-fold below that of RISC. Reactions were incubated at 37°C. At select time points, 5 μL of binding reaction was applied to stacked filter membrane discs, followed by 100 μL of ice-cold filter-binding wash buffer. The filter membrane discs were then quantified in the same way as in titration filter-binding assays for RISC quantification.

The fractions of target bound across time points were then fit to an exponential equation by nonlinear least-squares regression in R using the Levenberg-Marquardt algorithm (nlsLM), for no more than 100 iterations:

$$F_{bound} = A \cdot (1 - e^{-k_{on} \cdot [RISC_T] \cdot t})$$

where F_{bound} represents the fraction of target bound, A represents the maximum fraction of target bound at the plateau, k_{on} represents the association rate constant in nM^{-1} s^{-1}, $[RISC_T]$ represents the total RISC concentration in nM, and t represents time in s. This equation approximates association rate k_{on}[RISC] to be k_{on} $[RISC_T]$ and dissociation to be negligible, as the concentration of RISC was in vast excess over both the target concentration and K_D of binding. A was initialized at 0.8 and limited to the range (0, 1), and k_{on} was initialized at 0.0333 nM^{-1} s^{-1} and limited to the numerical range (0, 1), where 1 nM^{-1} s^{-1} was the diffusion limit. For lsy-6, k_{on} was too fast to resolve even with the first time point measured, and was therefore ≥ 1 nM^{-1} s^{-1} (≥ 60 nM^{-1} min^{-1}).

Filter-binding of slicing reactions

Slicing reactions were prepared and incubated similarly as described. Instead of quenching the reactions, they were filtered through a single pre-equilibrated nitrocellulose membrane. Individual discs of nitrocellulose membrane filters were placed on a circular pedestal mounted on a vacuum manifold, set at approximately −20 kPa. 5 μL of reaction was applied to each filter membrane disc, immediately followed by 100 μL of ice-cold filter-binding wash buffer. The filtrate was collected and mixed with 11 μL of 3 M NaCl, 1 μL of 25 mg/mL yeast tRNA, 5 μL of GlycoBlue co-precipitant (Invitrogen, AM9516), and 320 μL of ethanol, and incubated at −80°C for at least 1 h. The nitrocellulose membrane was air-dried briefly, then incubated in 420 μL of Proteinase K elution solution (47.3 mM Tris-HCl pH 7.5, 47.3 mM NaCl, 9.46 mM EDTA, 0.946% [v./v.] SDS, 0.01 mg/mL yeast tRNA, 1 mg/mL Proteinase K [Invitrogen, 25530049]) at 65°C with shaking at 1,200 rpm for 45 min. RNA was isolated from the proteinase digestion eluate by extraction with phenol:chloroform:isoamyl alcohol

(25:24:1) (Sigma-Aldrich, P2069) and chloroform. The resultant aqueous phase was mixed with 40 µL of 3 M NaOAc, 2 µL of 2.5 mg/mL yeast tRNA, 5 µL of GlycoBlue co-precipitant, and 1000 µL of ethanol, and incubated at −80°C for at least 1 h. RNA species from the filtrate and membrane eluant were precipitated by centrifugation at 4°C, and dried RNA pellets were each resuspended in 15 µL of a 1:1 (by volume) mixture of Gel Loading Dye II and filter-binding buffer. Samples were denatured by incubating at 37°C with shaking at 1,200 rpm for 10 min, and run on a 15% urea-polyacrylamide gel. Gels were imaged and quantified as described previously.

Thermodynamic modeling of slicing kinetics for 16-bp targets

The relationship between fold change in k_{slice} for slicing 16-bp targets ($\Delta k_{\text{slice (16-bp/perfect)}}$) and predicted base-pairing energy at positions 9−12 was modeled as the following equation, where energy gained from base-pairing is used to overcome an energetic barrier to slicing, assuming the slicing kinetics of perfectly complementary targets correspond to the maximal rates:

$$\Delta k_{slice\ (\text{16-bp/perfect})} = \frac{k_{slice\ (\text{16-bp})}}{k_{slice\ (\text{perfect})}} = \frac{1}{e^{\frac{\Delta G^\circ{}_{9-12} + \Delta G^\circ{}_{thres}}{RT}} + 1}$$

where ΔG°_{9-12} represents the predicted base-pairing energy at positions 9−12, $\Delta G^\circ_{\text{thres}}$ represents the energetic threshold to be overcome by ΔG°_{9-12}, R represents the molar gas constant, and T represents the temperature at 310.15 K (37 °C). Data were fit to this equation in log-scale using nonlinear least-squares regression in R, using the Levenberg-Marquardt algorithm (nlsLM). $\Delta G^\circ_{\text{thres}}$ was initialized at 10 kcal mol^{-1}.

Hydroxyl-radical footprinting of AGO2^{D669A}–RNA complexes

Base-hydrolysis ladders were generated by incubating 30 nM of radiolabeled guide RNAs with 50 mM Na_2CO_3, in a total volume of 10 µL, at 90°C for 4 min, followed by quenching with 20 µL of ice-cold 90% (v./v.) gel-loading buffer and 100 mM Tris-HCl acid. RNase T1 ladders were generated by first preincubating 3 nM of radiolabeled guide RNAs with 5 mM EDTA, 0.75 mg/mL GlycoBlue, 0.025 mg/mL yeast tRNA, and 0.88X RNA Sequencing Buffer, in a total volume of 100 µL, at 50°C for 5 min, then at 25°C for 3 min. 1 µL of RNase T1 (Invitrogen, AM2283) was added and mixed, and the reaction incubated at 25°C for 20 min, before adding 10 µL of 1 M DTT and extracting the RNA using phenol:chloroform:isoamyl alcohol (25:24:1) and chloroform. The aqueous phase was mixed with 200 µL of the Precipitation/Inactivation Buffer provided with RNase T1, and incubated at −80°C for 1 h. After centrifugation, the precipitate was resuspended in 30 µL of Gel Loading Dye II and denatured at 90°C for 2 min.

To provide a normalization standard for maximum hydroxyl-radical reactivity, radiolabeled guide RNAs were purified from AGO2^{D669A}–guide complexes by phenol:chloroform:isoamyl alcohol (25:24:1) and precipitation. AGO2^{D669A}–guide complexes or naked guide RNAs were preincubated in storage buffer without glycerol at 37°C for 30 s or 2 min. Non-radiolabeled target RNAs were preincubated in slicing-reaction buffer at 37°C for 30 s or 2 min. AGO2^{D669A}–guide complexes were mixed with target RNAs in buffer to a total volume of 15 µL, with the final concentration of AGO2^{D669A}–guide at 2 nM and target at 8 nM. The binding reaction mix was incubated at 37°C for 30 min or 1 min. Meanwhile, Fenton's reagent was prepared in buffer on ice as two separate solutions for each reaction: Solution A, containing 14.7 mM EDTA, 13.3 mM ammonium iron(II) sulfate (Sigma-Aldrich, 09719), and 33.3 mM DTT; and Solution B, containing 1% (v./v.) hydrogen peroxide (Sigma-Aldrich, 216763), 45 mM HEPES pH 7.4, 250 mM KOAc, 4.5 mM $Mg(OAc)_2$, and 0.025% (v/.v.) IGEPAL CA-630. Solutions A and B were preincubated separately at 37 °C for 20 s. The binding reaction was first rapidly mixed with 3 µL of Solution B, and then immediately mixed with 2 µL of Solution A, to a final total volume of 20 µL. The final footprinting reaction condition contained 1.5 nM AGO2^{D669A}–guide or naked guide RNA, 6 nM target RNA, 18 mM HEPES pH 7.4, 100 mM KOAc, 1.2 mM $Mg(OAc)_2$, 0.015 mg/mL BSA, 0.0015 mg/mL yeast tRNA, 0.01 (v/.v.) IGEPAL CA-630, 8.75 mM DTT, 2.2 mM EDTA, 2 mM ammonium iron(II) sulfate, and 0.1% (v./v.) (29.5 mM) hydrogen peroxide. The footprinting reaction mix was incubated at 37°C for 2 min, before quenching with 5 µL of ice-cold 0.5 M sodium sulfite (Sigma-Aldrich, S0505) and incubating on ice for at least 5 min. To provide a normalization standard for minimum reactivity, a quenched reaction was generated in which the incubated binding reaction was mixed with a pre-quenched mix of Solutions A and B and sodium sulfite on ice. 25 µL of each quenched reaction mix was added to 455 µL of ice-cold 0.3 M NaCl, and RNA species were extracted by phenol:chloroform:isoamyl alcohol (25:24:1) and chloroform. The aqueous phase was mixed with 5 µL of 5 mg/mL linear acrylamide co-precipitant (Invitrogen, AM9520) and 1000 µL of ethanol for precipitation. Dried pellets were resuspended in 10 µL of 200 mM Tris-HCl acid, 75% (v./v.) Gel Loading Dye II, and 25 nM non-radiolabeled guide RNA. The excess non-radiolabeled guide RNA was included so that it would anneal with complementary target RNA in the mix, thereby displacing radiolabeled guide-RNA species that would otherwise be paired to target RNA. Samples were denatured at 60°C for 10 min, and then resolved on a 20% urea-polyacrylamide sequencing gel, alongside previously prepared radiolabeled ladders of the guide RNAs. Gels were imaged and quantified as described.

Reactivity values were normalized by linearly rescaling the value at each nucleotide position relative to the mean reactivities of quenched-reagent samples (set to 0) and naked-guide samples (set to 1). One replicate for miR-430a bound to a seed+supplementary pairing target was discarded due to denatured complex, as indicated by a uniform and substantially elevated reactivity across all nucleotide positions, half of which were > 2 standard deviations above the mean across replicates.

To calculate the fraction occupancy of the catalytic state at 1 min, the increase in reactivity at positions 9−11 after 30 min of incubation ($\Delta R_{30\ \mathrm{min}}$), comparing to the no-target sample values, was first used to infer the steady-state increase in reactivity corresponding to complete occupancy of the catalytic state conformation (ΔR_{max}), at each nucleotide position i:

$$\Delta R_{max,i} = \frac{\Delta R_{30\ min,i}}{1 - e^{-k_{slice}\cdot(30\ \mathrm{min})}}$$

where $\Delta R_{\mathrm{max},i} \approx \Delta R_{30\ \mathrm{min},i} \times 1.5$ for miR-430a (with this difference between $\Delta R_{\mathrm{max},i}$ and $\Delta R_{30\ \mathrm{min},I}$ inferred from its slow k_{slice} value), and $\Delta R_{\mathrm{max},i} \approx \Delta R_{30\ \mathrm{min},i}$ for the other three guides. The fraction occupancy of catalytic state conformation at 1 min ($F_{\mathrm{con\ (1\ min)}}$) was, therefore:

$$F_{con\ (1\ min),i} = \frac{\Delta R_{1\ min,i}}{\Delta R_{max,i}}$$

for each nucleotide position i. The value of $F_{\mathrm{con\ (1\ min)}}$ for each replicate was the mean of $F_{\mathrm{con\ (1\ min)},i}$ across positions 9−11.

Mass spectrometry of purified RISCs

10 ng of AGO2 protein from each RISC, as quantified by titration filter-binding, was denatured with 4X LDS sample buffer (Invitrogen, NP0007) and run on an SDS-polyacrylamide gel (NuPAGE 4 to 12%, Bis-Tris [Invitrogen, NP0322]) in MOPS buffer (Invitrogen, NP0001), according to manufacturer's instructions. Gels were stained with Imperial Blue Stain (Thermo Scientific, 24615). Bands corresponding to AGO2 were excised and cut into pieces, then stored in 50% (v./v.) methanol. Proteins were eluted, digested with trypsin, and run on the Thermo Scientific Orbitrap Elite mass spectrometer with a Waters NanoAcuity UPLC system. Alignment of peptides and identification of modifications were carried out using either the Proteome Discoverer (Thermo Fisher) or Mascot (Matrix Science) software, followed by Scaffold 5 (Proteome Software). The label-free total ion chromatogram (TIC) signal for each assigned peak was used for relative quantitative analyses.

Luciferase reporter assays for RNAi-mediated knockdown

Reporter plasmids each featured a pUC origin of replication, an ampicillin resistance gene, and two minimal CMV promoters in divergent directions, with a common enhancer element in between. One promoter expressed a firefly luciferase that was used for reporter normalization. The other promoter expressed the reporter construct that contained the slicing site. The cap-dependent translation of its first ORF, which harbored the slicing site, was regulated by an IRE in the mRNA 5′ UTR. The 22-nt-long perfectly complementary slicing site for each guide RNA was introduced in the first ORF as part of a 24-nt-long region that linked the two ORF regions, preserving the codon frame. For each guide and ORF context, the frame of the slicing site was chosen to avoid any stop codons, rare codons, or highly hydrophobic amino acid residues. To measure the abundance of the reporter transcript independently from the regulation by the IRE, a second ORF was placed after a downstream EMCV IRES. It expressed a NanoLuc luciferase with a C-terminal PEST degradation sequence from mouse ornithine decarboxylase.[86] The PEST degron destabilized the NanoLuc protein, enabling faster approach to steady-state reporting of the mRNA abundance after treatments. The entire reporter construct transcript was approximately 2 kb in length. Both mRNAs terminated with the SV40 polyadenylation-signal sequence.

Two reporter template plasmids without slicing sites were each constructed by Gibson assembly from six fragments, including those encoding 3xFLAG or 3xHA, sfGFP or $SUMO^{Eu1}$, EMCV IRES, NanoLuc, PEST degron, and a plasmid backbone containing the remaining elements, mixed in 5:2:2:2:2:1 ratio by molarity, using the NEBuilder HiFi DNA Assembly Master Mix (New England Biolabs, E2621), according to manufacturer's instructions. Gibson assembly fragments were generated by PCR using KAPA HiFi HotStart Ready Mix and relevant primers (Table S2) on plasmids containing the corresponding sequences. The IRE hairpin was added to one end of the plasmid backbone fragment via an extended PCR primer. After assembly of the parental plasmids, slicing sites were inserted as 24-bp sequences through site-directed mutagenesis by PCR (Table S2) to generate each of the eight resultant plasmid variants. Plasmid sequences were verified by Sanger sequencing.

Guide−passenger RNA duplexes for transfection were generated in the same way as those used for RISC assembly, but without any ^{32}P-radiolabeled guide RNAs. To direct the correct strand selection by AGO2[85] while minimizing variations in loading, identical mismatches were introduced in the duplex for the wildtype and mutant variants of each guide pair.

HeLa or HEK293T cells were cultured in DMEM supplemented with 10% FBS, at 37°C in 0.5% CO_2. HeLa cells were plated at 30% confluency, and HEK293T cells were

plated at 20% confluency, each in 96-well plates with 100 μL of media per well. Cells were transfected 24 h after plating, using Lipofectamine 2000, according to manufacturer's instructions. Each well of cells was co-transfected using 0.18 μL of Lipofectamine 2000, 60 ng of reporter plasmid, and 0.6 pmol of carrier lsy-6 duplex, with or without 1.2 pmol of the RNA duplex being tested, mixed in Opti-MEM to a total volume of 50 μL. After 7 h of transfection, cells were treated for iron control. Stock solutions of 26.3 mg/mL (40 mM) desferroxamine mesylate (DFO; Sigma Aldrich, D9533) or 40 mg/mL ferric ammonium citrate (FAC; Sigma Aldrich, F5879) were prepared from powder, dissolved in 50% (v./v.) DMSO, and stored at −20°C. Cells were treated with 50 μL of either 3.3 μg (5 nmol) of DFO or 2.5 μg of FAC mixed in DMEM supplemented with 10% FBS, bringing the final total volume of media in each well to 200 μL. After 17 h of treatment, cells were examined and harvested for luciferase assays.

Fluorescence from sfGFP in cells transfected with context-A reporters was imaged using the EVOS M7000 Imaging System (Invitrogen). Fluorescence microscopy images were analyzed using ImageJ 1.53n, with the display intensity set to the range of 800−1500 out of a 15-bit range (0−32767) uniformly across all images.

Luciferase assays were conducted using the Dual-Luciferase Reporter assay system (Promega, E1960) according to manufacturer's instructions. Cell lysates were transferred to a 96-well reading plate, and luminescence was measured using the GloMax Discover microplate reader (Promega) with the default parameters for dual-luciferase assays. Fifteen measurements of cell lysates without any expressed luciferase were used to estimate the background reading levels of firefly luciferase and NanoLuc luciferase, and the mean background for each was respectively subtracted from all experimental readings before analysis in R.

Analysis of RNA backbones in high-resolution structure models of AGO2−RNA complexes

Structure models were downloaded from the RCSB Protein Data Bank. RNA backbone dihedral angles were measured using the web 3DNA 2.0 server,[87] followed by analysis in R. RNA backbone conformer analyses were conducted using MolProbity 4.2.[88] Iterative-build composite electron density omit maps ($2mF_o - DF_c$) were calculated in PHENIX 1.20,[84] using the phenix.composite_omit_map command with no refinement, and rendered in PyMOL 2.4.1 at 1.6 σ for all models generated using crystallography.

Prediction of RNA secondary structure and base-pairing energy

Minimum free energy secondary structures and corresponding predicted standard free energy ($\Delta G°_{37°C}$) values for slicing target RNAs were predicted *in silico* using the RNAfold program in the ViennaRNA 2.0 package.[89] Standard free energy of secondary structure involving the seed-match region was approximated by multiplying the total predicted standard free energy by the fraction of total base-pairs located within the seed-match region. Predicted $\Delta G°_{37°C}$ of sequence regions pairing to their complement were calculated using the RNAcofold program in the ViennaRNA 2.0 package, with the base-pairing pattern constrained to perfect complementarity using the -C and --enforceConstraint parameters, corrected for the initiation and/or symmetry energy penalties (4.09 and 0.43 kcal mol^{-1}, respectively[90]) when imposed.

Data and code availability

All code used for data analysis and graphing is available at https://github.com/wyppeter/AGO2_slicing_2023.

SUPPLEMENTAL INFORMATION

Table S1. Fitted parameters of slicing kinetics with different guides and targets, related to Figures 1, 2, 4, and 5

Table S2. Oligonucleotides used in this study, related to Methods

Supplemental Figures S1−S7. See Supplemental Figures and Legends

ACKNOWLEDGEMENTS

We thank S. E. McGeary, D. H. Lin, T. M. Pham, K. Xiang, and others in the Bartel laboratory for helpful discussions. We thank S.E.M., T.M.P., D. Briskin, and M. Hall for several purified RISCs. We thank the Whitehead Proteomics Core for conducting mass spectrometry and some of the associated analyses. This work was supported by a grant from the NIH. D.P.B. is an investigator of the Howard Hughes Medical Institute.

AUTHOR CONTRIBUTIONS

P.Y.W. and D.P.B. conceived the project, designed the study, and wrote the manuscript. P.Y.W. performed the experiments and data analyses.

DECLARATION OF INTERESTS

D.P.B. has equity in Alnylam Pharmaceuticals, where he is a co-founder and advisor. P.Y.W. declares no competing interests.

REFERENCES

1. Swarts, D.C., Makarova, K., Wang, Y., Nakanishi, K., Ketting, R.F., Koonin, E.V., Patel, D.J., and van der Oost, J. (2014). The evolutionary journey of Argonaute proteins. Nat. Struct. Mol. Biol. *21*, 743–753. 10.1038/nsmb.2879.
2. Bartel, D.P. (2018). Metazoan MicroRNAs. Cell *173*, 20–51. 10.1016/j.cell.2018.03.006.
3. Tomari, Y., and Zamore, P.D. (2005). Perspective: machines for RNAi. Genes Dev. *19*, 517–529. 10.1101/gad.1284105.
4. Wilson, R.C., and Doudna, J.A. (2013). Molecular Mechanisms of RNA Interference. Annu. Rev. Biophys. *42*, 217–239. 10.1146/annurev-biophys-083012-130404.
5. Bartel, D.P. (2004). MicroRNAs: Genomics, Biogenesis, Mechanism, and Function. Cell *116*, 281–297. 10.1016/S0092-8674(04)00045-5.
6. Elbashir, S.M., Harborth, J., Lendeckel, W., Yalcin, A., Weber, K., and Tuschl, T. (2001). Duplexes of 21-nucleotide RNAs mediate RNA interference in cultured mammalian cells. Nature *411*, 494–498. 10.1038/35078107.
7. Doench, J.G. (2003). siRNAs can function as miRNAs. Genes Dev. *17*, 438–442. 10.1101/gad.1064703.
8. Hutvágner, G., and Zamore, P.D. (2002). A microRNA in a Multiple-Turnover RNAi Enzyme Complex. Science *297*, 2056–2060. 10.1126/science.1073827.
9. Jonas, S., and Izaurralde, E. (2015). Towards a molecular understanding of microRNA-mediated gene silencing. Nat. Rev. Genet. *16*, 421–433. 10.1038/nrg3965.
10. Liu, J., Carmell, M.A., Rivas, F.V., Marsden, C.G., Thomson, J.M., Song, J.-J., Hammond, S.M., Joshua-Tor, L., and Hannon, G.J. (2004). Argonaute2 Is the Catalytic Engine of Mammalian RNAi. Science *305*, 1437–1441. 10.1126/science.1102513.
11. Orban, T.I., and Izaurralde, E. (2005). Decay of mRNAs targeted by RISC requires XRN1, the Ski complex, and the exosome. RNA *11*, 459–469. 10.1261/rna.7231505.

12. Meister, G., Landthaler, M., Patkaniowska, A., Dorsett, Y., Teng, G., and Tuschl, T. (2004). Human Argonaute2 Mediates RNA Cleavage Targeted by miRNAs and siRNAs. Mol. Cell *15*, 185–197. 10.1016/j.molcel.2004.07.007.

13. Rivas, F.V., Tolia, N.H., Song, J.-J., Aragon, J.P., Liu, J., Hannon, G.J., and Joshua-Tor, L. (2005). Purified Argonaute2 and an siRNA form recombinant human RISC. Nat. Struct. Mol. Biol. *12*, 340–349. 10.1038/nsmb918.

14. Park, M.S., Phan, H.-D., Busch, F., Hinckley, S.H., Brackbill, J.A., Wysocki, V.H., and Nakanishi, K. (2017). Human Argonaute3 has slicer activity. Nucleic Acids Res. *45*, 11867–11877. 10.1093/nar/gkx916.

15. Hansen, T.B., Wiklund, E.D., Bramsen, J.B., Villadsen, S.B., Statham, A.L., Clark, S.J., and Kjems, J. (2011). miRNA-dependent gene silencing involving Ago2-mediated cleavage of a circular antisense RNA. EMBO J. *30*, 4414–4422. 10.1038/emboj.2011.359.

16. Karginov, F.V., Cheloufi, S., Chong, M.M.W., Stark, A., Smith, A.D., and Hannon, G.J. (2010). Diverse Endonucleolytic Cleavage Sites in the Mammalian Transcriptome Depend upon MicroRNAs, Drosha, and Additional Nucleases. Mol. Cell *38*, 781–788. 10.1016/j.molcel.2010.06.001.

17. Shin, C., Nam, J.-W., Farh, K.K.-H., Chiang, H.R., Shkumatava, A., and Bartel, D.P. (2010). Expanding the MicroRNA Targeting Code: Functional Sites with Centered Pairing. Mol. Cell *38*, 789–802. 10.1016/j.molcel.2010.06.005.

18. Yekta, S. (2004). MicroRNA-Directed Cleavage of HOXB8 mRNA. Science *304*, 594–596. 10.1126/science.1097434.

19. Stein, P., Rozhkov, N.V., Li, F., Cárdenas, F.L., Davydenk, O., Vandivier, L.E., Gregory, B.D., Hannon, G.J., and Schultz, R.M. (2015). Essential Role for Endogenous siRNAs during Meiosis in Mouse Oocytes. PLOS Genet. *11*, e1005013. 10.1371/journal.pgen.1005013.

20. Cheloufi, S., Dos Santos, C.O., Chong, M.M.W., and Hannon, G.J. (2010). A dicer-independent miRNA biogenesis pathway that requires Ago catalysis. Nature *465*, 584–589. 10.1038/nature09092.

21. Cifuentes, D., Xue, H., Taylor, D.W., Patnode, H., Mishima, Y., Cheloufi, S., Ma, E., Mane, S., Hannon, G.J., Lawson, N.D., et al. (2010). A Novel miRNA Processing Pathway Independent of Dicer Requires Argonaute2 Catalytic Activity. Science *328*, 1694–1698. 10.1126/science.1190809.

22. Jee, D., Yang, J.-S., Park, S.-M., Farmer, D.T., Wen, J., Chou, T., Chow, A., McManus, M.T., Kharas, M.G., and Lai, E.C. (2018). Dual Strategies for

Argonaute2-Mediated Biogenesis of Erythroid miRNAs Underlie Conserved Requirements for Slicing in Mammals. Mol. Cell *69*, 265-278.e6. 10.1016/j.molcel.2017.12.027.

23. Yang, J.-S., and Lai, E.C. (2010). Dicer-independent, Ago2-mediated microRNA biogenesis in vertebrates. Cell Cycle *9*, 4455–4460. 10.4161/cc.9.22.13958.
24. Matranga, C., Tomari, Y., Shin, C., Bartel, D.P., and Zamore, P.D. (2005). Passenger-Strand Cleavage Facilitates Assembly of siRNA into Ago2-Containing RNAi Enzyme Complexes. Cell *123*, 607–620. 10.1016/j.cell.2005.08.044.
25. Miyoshi, K., Tsukumo, H., Nagami, T., Siomi, H., and Siomi, M.C. (2005). Slicer function of Drosophila Argonautes and its involvement in RISC formation. Genes Dev. *19*, 2837–2848. 10.1101/gad.1370605.
26. Leuschner, P.J.F., Ameres, S.L., Kueng, S., and Martinez, J. (2006). Cleavage of the siRNA passenger strand during RISC assembly in human cells. EMBO Rep. *7*, 314–320. 10.1038/sj.embor.7400637.
27. Friedrich, M., and Aigner, A. (2022). Therapeutic siRNA: State-of-the-Art and Future Perspectives. BioDrugs *36*, 549–571. 10.1007/s40259-022-00549-3.
28. Bartel, D.P. (2009). MicroRNAs: Target Recognition and Regulatory Functions. Cell *136*, 215–233. 10.1016/j.cell.2009.01.002.
29. Lewis, B.P., Shih, I., Jones-Rhoades, M.W., Bartel, D.P., and Burge, C.B. (2003). Prediction of Mammalian MicroRNA Targets. Cell *115*, 787–798. 10.1016/S0092-8674(03)01018-3.
30. Wang, Y., Juranek, S., Li, H., Sheng, G., Wardle, G.S., Tuschl, T., and Patel, D.J. (2009). Nucleation, propagation and cleavage of target RNAs in Ago silencing complexes. Nature *461*, 754–761. 10.1038/nature08434.
31. Chandradoss, S.D., Schirle, N.T., Szczepaniak, M., MacRae, I.J., and Joo, C. (2015). A Dynamic Search Process Underlies MicroRNA Targeting. Cell *162*, 96–107. 10.1016/j.cell.2015.06.032.
32. Jo, M.H., Shin, S., Jung, S.-R., Kim, E., Song, J.-J., and Hohng, S. (2015). Human Argonaute 2 Has Diverse Reaction Pathways on Target RNAs. Mol. Cell *59*, 117–124. 10.1016/j.molcel.2015.04.027.
33. Klum, S.M., Chandradoss, S.D., Schirle, N.T., Joo, C., and MacRae, I.J. (2018). Helix-7 in Argonaute2 shapes the microRNA seed region for rapid target recognition. EMBO J. *37*, 75–88. 10.15252/embj.201796474.
34. Salomon, W.E., Jolly, S.M., Moore, M.J., Zamore, P.D., and Serebrov, V. (2015). Single-Molecule Imaging Reveals that Argonaute Reshapes the Binding

Properties of Its Nucleic Acid Guides. Cell *162*, 84–95. 10.1016/j.cell.2015.06.029.

35. Sheu-Gruttadauria, J., Xiao, Y., Gebert, L.F., and MacRae, I.J. (2019). Beyond the seed: structural basis for supplementary microRNA targeting by human Argonaute2. EMBO J., e101153. 10.15252/embj.2018101153.
36. Xiao, Y., Maeda, S., Otomo, T., and MacRae, I.J. (2023). Structural basis for RNA slicing by a plant Argonaute. Nat. Struct. Mol. Biol., doi:10.1038/s41594-023-00989-7. 10.1038/s41594-023-00989-7.
37. Dayeh, D.M., Kruithoff, B.C., and Nakanishi, K. (2018). Structural and functional analyses reveal the contributions of the C- and N-lobes of Argonaute protein to selectivity of RNA target cleavage. J. Biol. Chem. *293*, 6308–6325. 10.1074/jbc.RA117.001051.
38. Hur, J.K., Zinchenko, M.K., Djuranovic, S., and Green, R. (2013). Regulation of Argonaute Slicer Activity by Guide RNA 3′ End Interactions with the N-terminal Lobe. J. Biol. Chem. *288*, 7829–7840. 10.1074/jbc.M112.441030.
39. Becker, W.R., Ober-Reynolds, B., Jouravleva, K., Jolly, S.M., Zamore, P.D., and Greenleaf, W.J. (2019). High-Throughput Analysis Reveals Rules for Target RNA Binding and Cleavage by AGO2. Mol. Cell *75*, 1–15. 10.1016/j.molcel.2019.06.012.
40. Deerberg, A., Willkomm, S., and Restle, T. (2013). Minimal mechanistic model of siRNA-dependent target RNA slicing by recombinant human Argonaute 2 protein. Proc. Natl. Acad. Sci. *110*, 17850–17855. 10.1073/pnas.1217838110.
41. Haley, B., and Zamore, P.D. (2004). Kinetic analysis of the RNAi enzyme complex. Nat. Struct. Mol. Biol. *11*, 599–606. 10.1038/nsmb780.
42. Wee, L.M., Flores-Jasso, C.F., Salomon, W.E., and Zamore, P.D. (2012). Argonaute Divides Its RNA Guide into Domains with Distinct Functions and RNA-Binding Properties. Cell *151*, 1055–1067. 10.1016/j.cell.2012.10.036.
43. Chen, G.R., Sive, H., and Bartel, D.P. (2017). A Seed Mismatch Enhances Argonaute2-Catalyzed Cleavage and Partially Rescues Severely Impaired Cleavage Found in Fish. Mol. Cell *68*, 1095-1107.e5. 10.1016/j.molcel.2017.11.032.
44. McGeary, S.E., Lin, K.S., Shi, C.Y., Pham, T.M., Bisaria, N., Kelley, G.M., and Bartel, D.P. (2019). The biochemical basis of microRNA targeting efficacy. Science *366*, eaav1741. 10.1126/science.aav1741.

45. Flores-Jasso, C.F., Salomon, W.E., and Zamore, P.D. (2013). Rapid and specific purification of Argonaute-small RNA complexes from crude cell lysates. RNA *19*, 271–279. 10.1261/rna.036921.112.

46. Ameres, S.L., Martinez, J., and Schroeder, R. (2007). Molecular Basis for Target RNA Recognition and Cleavage by Human RISC. Cell *130*, 101–112. 10.1016/j.cell.2007.04.037.

47. Brown, K.M., Chu, C., and Rana, T.M. (2005). Target accessibility dictates the potency of human RISC. Nat. Struct. Mol. Biol. *12*, 469–470. 10.1038/nsmb931.

48. Grimson, A., Farh, K.K.-H., Johnston, W.K., Garrett-Engele, P., Lim, L.P., and Bartel, D.P. (2007). MicroRNA Targeting Specificity in Mammals: Determinants beyond Seed Pairing. Mol. Cell *27*, 91–105. 10.1016/j.molcel.2007.06.017.

49. Agarwal, V., Bell, G.W., Nam, J.-W., and Bartel, D.P. (2015). Predicting effective microRNA target sites in mammalian mRNAs. eLife *4*, e05005. 10.7554/eLife.05005.

50. Horman, S.R., Janas, M.M., Litterst, C., Wang, B., MacRae, I.J., Sever, M.J., Morrissey, D.V., Graves, P., Luo, B., Umesalma, S., et al. (2013). Akt-Mediated Phosphorylation of Argonaute 2 Downregulates Cleavage and Upregulates Translational Repression of MicroRNA Targets. Mol. Cell *50*, 356–367. 10.1016/j.molcel.2013.03.015.

51. Reynolds, A., Leake, D., Boese, Q., Scaringe, S., Marshall, W.S., and Khvorova, A. (2004). Rational siRNA design for RNA interference. Nat. Biotechnol. *22*, 326–330. 10.1038/nbt936.

52. Tomari, Y., Matranga, C., Haley, B., Martinez, N., and Zamore, P.D. (2004). A Protein Sensor for siRNA Asymmetry. Science *306*, 1377–1380. 10.1126/science.1102755.

53. Hu, H., Yan, Z., Xu, Y., Hu, H., Menzel, C., Zhou, Y., Chen, W., and Khaitovich, P. (2009). Sequence features associated with microRNA strand selection in humans and flies. BMC Genomics *10*, 413. 10.1186/1471-2164-10-413.

54. Tafer, H., Ameres, S.L., Obernosterer, G., Gebeshuber, C.A., Schroeder, R., Martinez, J., and Hofacker, I.L. (2008). The impact of target site accessibility on the design of effective siRNAs. Nat. Biotechnol. *26*, 578–583. 10.1038/nbt1404.

55. Hentze, M.W., Caughman, S.W., Rouault, T.A., Barriocanal, J.G., Dancis, A., Harford, J.B., and Klausner, R.D. (1987). Identification of the Iron-Responsive Element for the Translational Regulation of Human Ferritin mRNA. Science *238*, 1570–1573. 10.1126/science.3685996.

56. Gu, S., Jin, L., Zhang, F., Sarnow, P., and Kay, M.A. (2009). Biological basis for restriction of microRNA targets to the 3′ untranslated region in mammalian mRNAs. Nat. Struct. Mol. Biol. *16*, 144–150. 10.1038/nsmb.1552.

57. Mayr, C., and Bartel, D.P. (2009). Widespread Shortening of 3′UTRs by Alternative Cleavage and Polyadenylation Activates Oncogenes in Cancer Cells. Cell *138*, 673–684. 10.1016/j.cell.2009.06.016.

58. Ruijtenberg, S., Sonneveld, S., Cui, T.J., Logister, I., de Steenwinkel, D., Xiao, Y., MacRae, I.J., Joo, C., and Tanenbaum, M.E. (2020). mRNA structural dynamics shape Argonaute-target interactions. Nat. Struct. Mol. Biol. *27*, 790–801. 10.1038/s41594-020-0461-1.

59. Schirle, N.T., Sheu-Gruttadauria, J., and MacRae, I.J. (2014). Structural basis for microRNA targeting. Science *346*, 608–613. 10.1126/science.1258040.

60. Sheu-Gruttadauria, J., Pawlica, P., Klum, S.M., Wang, S., Yario, T.A., Schirle Oakdale, N.T., Steitz, J.A., and MacRae, I.J. (2019). Structural Basis for Target-Directed MicroRNA Degradation. Mol. Cell *75*, 1243-1255.e7. 10.1016/j.molcel.2019.06.019.

61. Egli, M., Schlegel, M.K., and Manoharan, M. (2023). Acyclic (S)-glycol nucleic acid (S-GNA) modification of siRNAs improves the safety of RNAi therapeutics while maintaining potency. RNA *29*, 402–414. 10.1261/rna.079526.122.

62. Schlegel, M.K., Foster, D.J., Kel'in, A.V., Zlatev, I., Bisbe, A., Jayaraman, M., Lackey, J.G., Rajeev, K.G., Charissé, K., Harp, J., et al. (2017). Chirality Dependent Potency Enhancement and Structural Impact of Glycol Nucleic Acid Modification on siRNA. J. Am. Chem. Soc. *139*, 8537–8546. 10.1021/jacs.7b02694.

63. Arif, A., Bailey, S., Izumi, N., Anzelon, T.A., Ozata, D.M., Andersson, C., Gainetdinov, I., MacRae, I.J., Tomari, Y., and Zamore, P.D. (2022). GTSF1 accelerates target RNA cleavage by PIWI-clade Argonaute proteins. Nature *608*, 618–625. 10.1038/s41586-022-05009-0.

64. Willkomm, S., Jakob, L., Kramm, K., Graus, V., Neumeier, J., Meister, G., and Grohmann, D. (2022). Single-molecule FRET uncovers hidden conformations and dynamics of human Argonaute 2. Nat. Commun. *13*, 3825. 10.1038/s41467-022-31480-4.

65. Nilsen, T.W. (2014). Mapping RNA–Protein Interactions Using Hydroxyl-Radical Footprinting. Cold Spring Harb. Protoc. *2014*, pdb.prot080952. 10.1101/pdb.prot080952.

66. Frank, F., Sonenberg, N., and Nagar, B. (2010). Structural basis for 5′-nucleotide base-specific recognition of guide RNA by human AGO2. Nature *465*, 818–822. 10.1038/nature09039.

67. Elbashir, S.M., Lendeckel, W., and Tuschl, T. (2001). RNA interference is mediated by 21- and 22-nucleotide RNAs. Genes Dev. *15*, 188–200. 10.1101/gad.862301.

68. McGeary, S.E., Bisaria, N., Pham, T.M., Wang, P.Y., and Bartel, D.P. (2022). MicroRNA 3′-compensatory pairing occurs through two binding modes, with affinity shaped by nucleotide identity and position. eLife *11*, e69803. 10.7554/eLife.69803.

69. Schofield, J.A., Duffy, E.E., Kiefer, L., Sullivan, M.C., and Simon, M.D. (2018). TimeLapse-seq: adding a temporal dimension to RNA sequencing through nucleoside recoding. Nat. Methods *15*, 221–225. 10.1038/nmeth.4582.

70. Wu, Q., Medina, S.G., Kushawah, G., DeVore, M.L., Castellano, L.A., Hand, J.M., Wright, M., and Bazzini, A.A. (2019). Translation affects mRNA stability in a codon-dependent manner in human cells. eLife *8*, e45396. 10.7554/eLife.45396.

71. Yang, E., Nimwegen, E. van, Zavolan, M., Rajewsky, N., Schroeder, M., Magnasco, M., and Darnell, J.E. (2003). Decay Rates of Human mRNAs: Correlation With Functional Characteristics and Sequence Attributes. Genome Res. *13*, 1863–1872. 10.1101/gr.1272403.

72. Song, G., Chen, H., Sheng, G., Wang, Y., and Lou, J. (2018). Argonaute Facilitates the Lateral Diffusion of the Guide along Its Target and Prevents the Guide from Being Pushed Away by the Ribosome. Biochemistry *57*, 2179–2183. 10.1021/acs.biochem.8b00213.

73. Filbeck, S., Cerullo, F., Pfeffer, S., and Joazeiro, C.A.P. (2022). Ribosome-associated quality-control mechanisms from bacteria to humans. Mol. Cell *82*, 1451–1466. 10.1016/j.molcel.2022.03.038.

74. Liang, X., Nichols, J.G., Hsu, C.-W., Vickers, T.A., and Crooke, S.T. (2019). mRNA levels can be reduced by antisense oligonucleotides via no-go decay pathway. Nucleic Acids Res. *47*, 6900–6916. 10.1093/nar/gkz500.

75. Elkayam, E., Faehnle, C.R., Morales, M., Sun, J., Li, H., and Joshua-Tor, L. (2017). Multivalent Recruitment of Human Argonaute by GW182. Mol. Cell *67*, 646-658.e3. 10.1016/j.molcel.2017.07.007.

76. Ameres, S.L., Horwich, M.D., Hung, J.-H., Xu, J., Ghildiyal, M., Weng, Z., and Zamore, P.D. (2010). Target RNA–Directed Trimming and Tailing of Small Silencing RNAs. Science *328*, 1534–1539. 10.1126/science.1187058.

77. Han, J., and Mendell, J.T. (2023). MicroRNA turnover: a tale of tailing, trimming, and targets. Trends Biochem. Sci. *48*, 26–39. 10.1016/j.tibs.2022.06.005.

78. Masliah, G., Barraud, P., and Allain, F.H.-T. (2013). RNA recognition by double-stranded RNA binding domains: a matter of shape and sequence. Cell. Mol. Life Sci. *70*, 1875–1895. 10.1007/s00018-012-1119-x.

79. Faehnle, C.R., Elkayam, E., Haase, A.D., Hannon, G.J., and Joshua-Tor, L. (2013). The Making of a Slicer: Activation of Human Argonaute-1. Cell Rep. *3*, 1901–1909. 10.1016/j.celrep.2013.05.033.

80. Schürmann, N., Trabuco, L.G., Bender, C., Russell, R.B., and Grimm, D. (2013). Molecular dissection of human Argonaute proteins by DNA shuffling. Nat. Struct. Mol. Biol. *20*, 818–826. 10.1038/nsmb.2607.

81. Pédelacq, J.-D., Cabantous, S., Tran, T., Terwilliger, T.C., and Waldo, G.S. (2006). Engineering and characterization of a superfolder green fluorescent protein. Nat. Biotechnol. *24*, 79–88. 10.1038/nbt1172.

82. Vera Rodriguez, A., Frey, S., and Görlich, D. (2019). Engineered SUMO/protease system identifies Pdr6 as a bidirectional nuclear transport receptor. J. Cell Biol. *218*, 2006–2020. 10.1083/jcb.201812091.

83. Richardson, J.S., Schneider, B., Murray, L.W., Kapral, G.J., Immormino, R.M., Headd, J.J., Richardson, D.C., Ham, D., Hershkovits, E., Williams, L.D., et al. (2008). RNA backbone: Consensus all-angle conformers and modular string nomenclature (an RNA Ontology Consortium contribution). RNA *14*, 465–481. 10.1261/rna.657708.

84. Terwilliger, T.C., Grosse-Kunstleve, R.W., Afonine, P.V., Moriarty, N.W., Adams, P.D., Read, R.J., Zwart, P.H., and Hung, L.-W. (2008). Iterative-build OMIT maps: map improvement by iterative model building and refinement without model bias. Acta Crystallogr. D Biol. Crystallogr. *64*, 515–524. 10.1107/S0907444908004319.

85. Elbashir, S.M., Martinez, J., Patkaniowska, A., Lendeckel, W., and Tuschl, T. (2001). Functional anatomy of siRNAs for mediating efficient RNAi in Drosophila melanogaster embryo lysate. EMBO J. *20*, 6877–6888. 10.1093/emboj/20.23.6877.

86. Philippe, L., van den Elzen, A.M.G., Watson, M.J., and Thoreen, C.C. (2020). Global analysis of LARP1 translation targets reveals tunable and dynamic features of 5′ TOP motifs. Proc. Natl. Acad. Sci. *117*, 5319–5328. 10.1073/pnas.1912864117.

87. Zheng, G., Lu, X.-J., and Olson, W.K. (2009). Web 3DNA—a web server for the analysis, reconstruction, and visualization of three-dimensional nucleic-acid structures. Nucleic Acids Res. *37*, W240–W246. 10.1093/nar/gkp358.

88. Chen, V.B., Arendall, W.B., Headd, J.J., Keedy, D.A., Immormino, R.M., Kapral, G.J., Murray, L.W., Richardson, J.S., and Richardson, D.C. (2010). MolProbity: all-atom structure validation for macromolecular crystallography. Acta Crystallogr. D Biol. Crystallogr. *66*, 12–21. 10.1107/S0907444909042073.

89. Lorenz, R., Bernhart, S.H., Höner zu Siederdissen, C., Tafer, H., Flamm, C., Stadler, P.F., and Hofacker, I.L. (2011). ViennaRNA Package 2.0. Algorithms Mol. Biol. *6*, 26. 10.1186/1748-7188-6-26.

90. Mathews, D.H., Disney, M.D., Childs, J.L., Schroeder, S.J., Zuker, M., and Turner, D.H. (2004). Incorporating chemical modification constraints into a dynamic programming algorithm for prediction of RNA secondary structure. Proc. Natl. Acad. Sci. *101*, 7287–7292. 10.1073/pnas.0401799101.

91. De, N., Young, L., Lau, P.-W., Meisner, N.-C., Morrissey, D.V., and MacRae, I.J. (2013). Highly Complementary Target RNAs Promote Release of Guide RNAs from Human Argonaute2. Mol. Cell *50*, 344–355. 10.1016/j.molcel.2013.04.001.